Toward Verification of the $\gamma - Re_{\theta t}$ Transition Model in OVERFLOW and FUN3D

Balaji Shankar Venkatachari*
National Institute of Aerospace, Hampton, VA 23666

Marie F. Denison†
NASA Ames Research Center, Moffet Field, CA 94035

Preethi V. Mysore‡, Nathaniel J. Hildebrand,§ and Meelan M. Choudhari**
NASA Langley Research Center, Hampton, VA 23681

Abstract

The results of an ongoing assessment of the transition modeling capability in NASA's OVERFLOW and FUN3D codes are presented, with a focus on the Langtry-Menter γ-$Re_{\theta t}$ transition model in combination with the shear-stress transport (SST) turbulence model. While the effect of numerics and boundary conditions on the accuracy and iterative convergence of RANS solutions for fully turbulent flows has been well documented, especially in the context of canonical flow configurations, the same cannot be said for transport-equation-based transition models coupled with RANS-based turbulence models. Given the criticality of transition modeling for new aircraft design and optimization, there has been a renewed focus on the accuracy of such transition models and their inconsistent implementation across different flow solvers as seen from the AIAA and NATO-AVT workshops. In this work, we aim to establish the verification of such models via these two well established CFD codes with different numerics. The goal is to produce high-quality data, such as grids, solutions, and other auxiliary data, that may be utilized for code verification by others in the CFD community. As a first step, the work reported here is focused on the Langtry-Menter transition model as applied to two simple 2D configurations, namely the flat plate, and the NLF-0416, respectively. The paper also highlights how the boundary conditions and baseline turbulence model can affect the solutions from the SST-based Langtry-Menter transition model. A preliminary evaluation of the automatic mesh adaption capabilities of these solvers and potential benefits for flow configurations involving a mix of laminar, transitional, and fully turbulent flows is also reported.

Nomenclature

c	=	chord length [m]
C_D	=	drag coefficient
C_{DV}	=	viscous component of drag coefficient
C_f	=	skin-friction coefficient
C_p	=	surface pressure coefficient
d	=	distance to the nearest wall [m]
h	=	grid spacing parameter, $1/\sqrt{N}$
k	=	turbulent kinetic energy [kg m^2 s^{-2}]
M	=	Mach number
N	=	Total number of grid points
Re	=	unit Reynolds number [m^{-1}]

*Sr. Research Engineer, Email: balaji.s.venkatachari@nasa.gov, Senior member, AIAA
†Research Aerospace Engineer, NASA Advanced Supercomputing Division, marie.f.denison@nasa.gov, Senior member, AIAA.
‡Undergraduate Student, Computational AeroSciences Branch, Email: preethi.v.mysore@nasa.gov
§Aerospace Technologist, Computational AeroSciences Branch, Email: nathaniel.j.hildebrand@nasa.gov, AIAA Member
**Aerospace Technologist, Computational AeroSciences Branch, Email: m.m.choudhari@nasa.gov, Fellow, AIAA

Re_c = Chord-based Reynolds number
$\widetilde{Re_{\theta t}}$ = transition onset momentum thickness Reynolds number based on local boundary-layer edge conditions
S_{ij} = Strain-rate tensor, $0.5\left(\frac{\partial u_i}{\partial x_j}+\frac{\partial u_j}{\partial x_i}\right)$ [s^{-1}]
T = temperature [K]
Tu = freestream turbulence intensity
(u,v,w) = streamwise, wall-normal, and spanwise velocity components [m s^{-1}]
(x, y, z) = Cartesian coordinates [m]
x/c = chordwise coordinate scaled by reference chord length
y^+ = near wall grid spacing in wall units
α = angle of attack [deg]
γ = intermittency
μ = dynamic viscosity [kg/(m.s)]
μ_t = turbulent eddy viscosity [kg/(m.s)]
ρ = density [kg m^{-3}]
ω = specific turbulence dissipation rate [s^{-1}]

Subscripts
∞ = farfield reference state

Abbreviations
CFD = computational fluid dynamics
LM = Langtry-Menter
RANS = Reynolds-averaged Navier-Stokes
SST = shear stress transport
V&V = verification and validation

I. Introduction

Natural laminar flow is seen as a significant contributor to the pursuit of sustainable aviation and greener air transport technologies. As a result, NASA has recently supported two major experimental campaigns related to the topic of natural laminar flow wings, namely, the common research model with natural laminar flow wing [1,2] and the slotted airfoil design [3]. However, one of the main challenges in designing such wings is the capability to accurately predict viscous flows with laminar-to-turbulent boundary layer transition, which has been listed as a critical and pacing item for computational fluid dynamics (CFD) in the NASA CFD Vision 2030 [4] study.

The most accurate way to predict the complete set of physical processes of the transition of a laminar boundary layer into turbulent flow will be through direct numerical simulations and wall-resolved large-eddy simulations. However, due to reasons of excessive computational cost alone, these methods will remain impractical for the regular CFD user at least for the next decade. The most widely used approaches for the prediction of transition onset locations in aircraft design include semiempirical correlations based on linear stability theory (LST), such as the e^N method [5,6] or the parabolized stability equations (PSE) [7]. However, accurate prediction of the linear stability characteristics in conjunction with a coupled computation of the laminar, transitional, and fully turbulent parts of the flowfield requires sufficiently well-resolved boundary layer profiles in the laminar parts of the flow, increasing the computational cost. This approach is also not easy to implement within the framework of modern CFD codes, which rely upon massive parallelization and the use of unstructured grids [8] that are not compatible with the global dependence of the stability characteristics in one or more spatial directions. Furthermore, the stability-theory suffers from a lack of robustness, and often requires an advanced understanding of the hydrodynamic stability theory that typical CFD users may not have. Although some work [9-12] is being done to overcome these restrictions, it has not matured enough to allow routine use. As an alternative,

surrogate models, such as those described in Refs. [13] and [14], based on the laminar flow information provided by the flow solver have been used in lieu of the direct computation of stability characteristics.

A majority of the CFD computations are already being performed using Reynolds-averaged Navier-Stokes (RANS) models, under the assumption that the flow is turbulent everywhere. RANS models are computationally efficient, easy to implement and thereby widely available in many CFD solvers. Consequently, the development and usage of RANS-based transition models has gained substantial traction in recent years (see Refs.[15]–[23]). These models incorporate information about the transition process into the RANS framework using only local information, instead of needing detailed boundary-layer profiles or integral boundary-layer parameters. They achieve this by solving additional transport equations and relying on correlations to determine the onset of transition, making it easy to be implemented in modern unstructured grid-based CFD codes. However, it may be noted that most of the RANS-based models perform adequately only in limited flow regimes as the correlations used within these models are derived from limited experiments and the approach truly does not account for the physics involved in the boundary-layer transition process.

Despite the above-mentioned limitations of the transport-equation-based transition models, they have been successful in modeling a range of transition scenarios, under limited speed regimes, initiated via linear instabilities of the boundary layer flow as well as through bypass mechanisms related to finite amplitude disturbances. Some of the commonly used models are the shear-stress transport (SST) (see Refs. [24], [25]) RANS model-based two-equation $\gamma - Re_{\theta t}$ model by Langtry and Menter [17], the Spalart-Almaras (SA) [26] model-based Amplification Transport Equation model developed by Coder and Maughmer [21] and subsequently extended by Coder [22], the model for bypass transition by Walter and Leylek [16], and the one-equation γ model by Menter [23].

Given the importance of laminar-to-turbulent boundary layer transition and the wide emerging use of RANS-based transition models, the accuracy of these models and verification of their implementations have been the focus of some recent workshops organized by AIAA[††] (1st AIAA transition prediction and modeling workshop) and NATO AVT-313 workgroups.[‡‡] One major conclusion from these workshops (see Eca et al. [27]) is that even for simple configurations there is a great scatter amongst results computed on the same family of grids from different codes that were all supposed to have the same implementation of a particular transition model even as the grid is refined. This observation could be a result of variety of causes, such as: (i) inadequate refinement of grids, (ii) inconsistency in transition model implementation, and (iii) influence of numerics and boundary conditions. While NASA's turbulence model resource[§§] has helped the CFD community improve the consistency, accuracy and validation of widely-used RANS turbulence models, we still do not have a similar resource for RANS-based transition models, and the above-mentioned workshops were first steps toward that objective. Thus, even though one may have verified the RANS turbulence models in their code, and the code developers may have carefully added the transition model into the code, if the transition model is implemented on a different variant of the turbulence model as opposed to the one it was originally supposed to be coupled with, it is possible to have widely different results. Hence, having proper documentation of the transition model implementations along with details on the specified inflow and other boundary conditions is necessary to help identify where the differences come from. I would also help with the proper assessment of these models and subsequently, the success of these workshops.

As a first step toward building a transition model equivalent of the NASA's turbulence modeling resource, where test cases, grids, results and details on model implementation necessary for verification and validation of the transition models are provided, the present work is built upon our contributions to the 1st AIAA transition prediction and modeling workshop focusing on code-to-code verification of the SST-based Langtry-Menter (LM) transition model as implemented in NASA's OVERFLOW [28] and FUN3D codes [29]. Given that the numerics and turbulence model implementations within these codes have been well established and verified, it is expected to provide a good platform to verify RANS-based transition models and establish a consistent starting point through which assessment of these models for more complex flows

[††] URL: https://transitionmodeling.larc.nasa.gov/workshop_i/ (last accessed April 29, 2022)
[‡‡] URL: http://web.tecnico.ulisboa.pt/ist12278/Workshop_AVT_313_2D_cases/Workshop_AVT_313_2D_cases.htm (last accessed April 29,2022)
[§§] URL:http://turbmodels.larc.nasa.gov (last accessed April 29, 2022)

can be carried out with confidence. As part of this verification exercise, we will be assessing if the LM model as implemented in these codes approaches the same results, in terms of metrics such as overall lift and drag coefficients and details regarding the transition zone, when the grid family made available by the AIAA committee was extended to generate solutions closer to their asymptotic limit. The assessment will be carried out in the context of a flat plate under two different freestream conditions based on the ERCOFTAC T3 Series of experiments [30,31] and for the NLF-0416 airfoil [32] under two different angles of attack.

In addition to the verification exercise, we will also explore the influence of specific model-related boundary conditions as well as variations to the baseline turbulence model, to demonstrate how they may affect the transition onset and overall result. We will also be performing a preliminary investigation of using mesh adaption techniques available within these solvers in the context of transition prediction as opposed to hand-crafted grids.

The paper is organized as follows. Section II provides a brief overview of the CFD solvers as well as some details on the LM model and the SST-2003 turbulence model that the LM model is coupled with. The findings of the verification exercise, as well as other test scenarios and mesh specifics, are provided in Section III. Section IV contains results from a limited investigation on the sensitivity of the results to model implementation specifics and boundary conditions, while section V offers preliminary results from two different approaches to mesh adaption in the context of transitional flows. Finally, concluding remarks are provided in Section VI.

II. Flow Solver

A short description of the two CFD solvers used in this work is provided in this section, along with selected details of the LM model.

A. OVERFLOW

Version 2.3b of the NASA OVERFLOW code [28] is an implicit, structured, overset grid Navier-Stokes solver that is capable of computing both time-accurate and steady-state solutions via a variety of options for the spatial as well as temporal discretizations. RANS-based transition models available in OVERFLOW 2.3b include: (i) the two-equation Langtry-Menter transition model (LM2009) [17] based on the 2003 version of Menter's SST RANS model [25], along with the modifications proposed by Langtry et al. [19] to account for crossflow induced transition (LM2015); (ii) Coder's 2017b version of the amplification factor transport (AFT2017b) equation-based model [22] that uses the SA model; and (iii) the SA-based Medida-Baeder transition model [18]. The LM2009 solutions presented here were obtained by running the OVERFLOW solver in steady-state mode using low-Mach preconditioning, the 3rd-order Roe upwind scheme [33] and the unfactored successive symmetric overrelaxation (SSOR) implicit solution algorithm [34-35]. Third-order discretization was utilized for the convective terms in all the transport equations, while the gradients were evaluated using second-order accurate discretization. Unless specified, no additional limiters were used.

B. FUN3D

The suite of codes known as FUN3D (see Refs. [29], [36]) is an unstructured node-centered upwind-biased implicit RANS flow solver. FUN3D uses a finite-volume method. The inviscid fluxes are calculated with a Roe-Riemann solver [33]. For second-order accuracy, the interface values are obtained by extrapolation of the centroidal values of the control volumes (based on gradients computed at the mesh vertices with an unweighted least-squares technique). The viscous fluxes are discretized in a manner that velocity gradients on dual faces are calculated with the Green-Gauss theorem. The convective terms of the turbulence equations are solved using a first-order spatial discretization scheme. Pseudotime integration is performed with a backward Euler scheme. The linear system of equations at each time step is numerically solved with a point implicit procedure or an implicit line relaxation scheme described in Nielsen et al. [37]. Currently, the two-equation LM2009 model along with modifications for crossflow induced transition is the only RANS-based transition model available within FUN3D.

C. SST-based- $\gamma - Re_{\theta t}$ model

The original Langtry-Menter $\gamma - Re_{\theta t}$ transition model, as described in Ref. [17], includes two transition related transport equations intended to be used in conjunction with the SST-2003 version of the Menter shear stress transport model [24]. The SST-2003 turbulence model is described by the following two equations for the transport of turbulence kinetic energy and specific turbulence dissipation rate.

$$\frac{\partial(\rho k)}{\partial t} + \frac{\partial(\rho u_j k)}{\partial x_j} = P_{\text{lim}} \; -\beta^* \rho \omega k \; + \frac{\partial}{\partial x_j}\left[(\mu + \sigma_k \mu_t)\frac{\partial k}{\partial x_j}\right] \tag{1}$$

$$\frac{\partial(\rho \omega)}{\partial t} + \frac{\partial(\rho u_j \omega)}{\partial x_j} = \frac{\alpha}{\nu_t} P_{\text{lim}} - \beta \rho \omega^2 \; + \frac{\partial}{\partial x_j}\left[(\mu + \sigma_\omega \mu_t)\frac{\partial \omega}{\partial x_j}\right] + 2(1 - F_1)\frac{\rho \sigma_{\omega 2}}{\omega}\frac{\partial k}{\partial x_j}\frac{\partial \omega}{\partial x_j} \tag{2}$$

In the above equations, P_{lim} is a limited version of the production term P, that is defined as:

$$P_{\text{lim}} = \min(P, 10\beta^* \rho \omega k) \tag{3}$$

$$P = \tau_{ij}\frac{\partial u_i}{\partial x_j} \tag{4}$$

$$\tau_{ij} = \mu_t\left(2S_{ij} - \frac{2}{3}\frac{\partial u_k}{\partial x_j}\delta_{ij}\right) - \frac{2}{3}\rho k \delta_{ij} \tag{5}$$

$$S_{ij} = \frac{1}{2}\left(\frac{\partial u_i}{\partial x_j} + \frac{\partial u_{ji}}{\partial x_i}\right). \tag{6}$$

The turbulent eddy viscosity is computed using

$$\mu_t = \frac{\rho a_1 k}{\max(a_1 \omega, S F_2)} \tag{7}$$

where the strain-invariant S is defined as

$$S = \sqrt{2 S_{ij} S_{ij}}\,. \tag{8}$$

Each of the constants used in the model is a blend of an inner (1) and outer (2) constant, calculated as:

$$\phi = F_1 \phi_1 + (1 - F_1)\phi_2 \tag{9}$$

where ϕ_1 represents the inner constant and ϕ_2 the outer constant. F_1 and F_2 are given by:

$$\begin{gathered} F_1 = \tanh\left(\arg_1^4\right) \\ \arg_1 = \min\left[max\left(\frac{\sqrt{k}}{\beta^* \omega d}, \frac{500\nu}{d^2 \omega}\right), \frac{4\rho\sigma_{\omega 2} k}{CD_{k\omega} d^2}\right] \\ CD_{k\omega} = nax\left(2\rho\sigma_{\omega 2}\frac{1}{\omega}\frac{\partial k}{\partial x_j}\frac{\partial \omega}{\partial x_j}, 10^{-10}\right) \\ F_2 = \tanh\left(\arg_2^4\right) \\ \arg_2 = max\left(2\frac{\sqrt{k}}{\beta^* \omega d}, \frac{500\nu}{d^2 \omega}\right) \end{gathered} \tag{10}$$

where d is the distance from the field point to the nearest wall. The constants are:

$$\begin{gathered}\alpha_1=\frac{5}{9};\ \ \alpha_2=0.44\\ \sigma_{k1}=0.85;\ \ \sigma_{\omega1}=0.5;\ \ \beta_1=0.075\\ \sigma_{k2}=1.0;\ \ \sigma_{\omega2}=0.856;\ \ \beta_2=0.0828\\ \beta^*=0.09;\ \ \kappa=0.41;\ \ a_1=0.31.\end{gathered} \tag{11}$$

Unlike the SA-based models, the two equation SST model requires the specification of the turbulence kinetic energy (TKE) and its decay rate as part of the boundary condition. The near-field value of the TKE has a strong influence on the location of the boundary-layer transition location and, hence, must be specified correctly. Currently, one approach to avoid the turbulence decay upstream of the body is to use the option of sustaining turbulence [38], while the other is to start with a higher than desired value of freestream turbulent intensity and allow it to decay. Both these approaches have their pros and cons and can deeply influence the behavior of the solution. When the option to sustain turbulence is used to prevent non-physical decay of turbulence variables in the freestream, Eqs. (1) and (2) are modified into the following form through addition of an extra term on the right-hand-side of the equation:

$$\frac{\partial(\rho k)}{\partial t}+\frac{\partial(\rho u_j k)}{\partial x_j}=P_{\text{lim}}\ -\beta^*\rho\omega k\ +\frac{\partial}{\partial x_j}\left[(\mu+\sigma_k\mu_t)\frac{\partial k}{\partial x_j}\right]+\beta^*\rho\omega_{amb}k_{amb} \tag{1a}$$

$$\frac{\partial(\rho\omega)}{\partial t}+\frac{\partial(\rho u_j\omega)}{\partial x_j}=\frac{\alpha}{\nu_t}P_{\text{lim}}-\beta\rho\omega^2\ +\frac{\partial}{\partial x_j}\left[(\mu+\sigma_\omega\mu_t)\frac{\partial\omega}{\partial x_j}\right]+2(1-F_1)\frac{\rho\sigma_{\omega2}}{\omega}\frac{\partial k}{\partial x_j}\frac{\partial\omega}{\partial x_j}+\beta\rho\omega_{amb}^2 \tag{2a}$$

where k_{amb} and ω_{amb} are the farfield boundary values of the turbulence variables. This modification is denoted as SST-sust2003, as per nomenclature suggested by the NASA turbulence modeling resource.

The transport equations for the intermittency and the surrogate "transition onset momentum-thickness Reynolds number," $\widetilde{Re_{\theta t}}$, that make up the LM model are given as:

$$\frac{\partial(\rho\gamma)}{\partial t}+\frac{\partial(\rho U_j\gamma)}{\partial x_j}=P_\gamma-E_\gamma+\frac{\partial}{\partial x_j}\left[\left(\mu+\frac{\mu_t}{\sigma_j}\right)\frac{\partial\gamma}{\partial x_j}\right] \tag{12}$$

$$\frac{\partial(\rho\widetilde{Re_{\theta t}})}{\partial t}+\frac{\partial(\rho U_j\widetilde{Re_{\theta t}})}{\partial x_j}=P_{\theta t}+\frac{\partial}{\partial x_j}\left[\sigma_{\theta t}(\mu+\mu_t)\frac{\partial\widetilde{Re_{\theta t}}}{\partial x_j}\right]. \tag{13}$$

The definitions of the production and destruction terms in the above two equations can be found in Ref. [17] or in the TMR webpage and involve several correlations. The transition model interacts with the SST-2003 model through modifications to the production and destruction terms in the turbulent kinetic energy transport equation and the blending function F_1 (Eq. (10|)), respectively. The modified turbulence kinetic energy transport equation without the sustaining term (Eq. (1)) is of the form:

$$\frac{\partial(\rho k)}{\partial t}+\frac{\partial(\rho u_j k)}{\partial x_j}=\tilde{P}\ -\widetilde{D}\ +\frac{\partial}{\partial x_j}\left[(\mu+\sigma_k\mu_t)\frac{\partial k}{\partial x_j}\right] \tag{1b}$$

where,

$$\tilde{P}=\gamma_{\text{eff}}\,P_{lim}\ ;\ \widetilde{D}=\min\left(\max(\gamma_{\text{eff}},0.1),1.0\right)\beta^*\rho\omega k \tag{14}$$

and

$$F_{1,mod}=\max(F_1,F_3)\ \ ;\ \ F_3=e^{-\left(\frac{R_y}{120}\right)8}\ \ ;\ \ R_y=\frac{\rho d\sqrt{k}}{\mu}. \tag{15}$$

The production term in the ω-equation is not modified.

III. Test Cases, Results, and Discussion

All of the results in this section are based on steady-state calculations using the Langtry-Menter transition model based on SST-2003. According to NASA's turbulence model resource, this model should be referred to as SST-2003-LM2009; nevertheless, for brevity, it will be abbreviated herein as simply the LM model, at least until specific variants of the model are used. Furthermore, all computations were performed until the *L2* norm of the mean flow residuals dropped below 10^{-8} or even lower where possible, and the force coefficients reached a plateau.

A. Flat Plate

As the first test case, subsonic flow over a two-dimensional zero-pressure-gradient flat plate with a sharp leading edge was computed for conditions that matched the experimental investigations corresponding to the T3A and T3A- condition [30-31] from the T3 series of test cases hosted by the ERCOFTAC (European Research Community on Flow, Turbulence and Combustion). The freestream conditions, the values of turbulence intensity and eddy-viscosity ratio imposed at the inflow boundary condition, and that measured at the leading edge of the plate are listed in Table 1. For the T3A case, the flow conditions used here correspond to those specified in the AIAA Transition Modeling and Prediction workshop, while the conditions for the T3A- case were taken to be those listed in the original ERCOFTAC publication. For both test cases, the levels of freestream turbulence and the eddy-viscosity specified at the inlet was such that one matched the measured freestream turbulence decay in the experiment using the analytic behavior of the SST model and the size of the domain. The results shown here using both CFD solvers were obtained without using the terms to sustain turbulence in the SST model.

Table 1. Flow conditions for the flat plate test cases.

Case	T3A	T3A-
Inlet Velocity (m/s)	69.44	19.8
Density (kg/m^3)	0.053	1.2
$\mu \times 10^{-5}$ (kg/[m.s])	1.85	1.79
Freestream Temperature (K)	300.0	288.17
Mach Number	0.20	0.058
Unit Reynolds number (/m)	2.000E5	1.328E6
μ_t/μ at inlet	11.9	9.0
Tu (%) at inlet	5.855	1.0
Tu (%) at the leading edge	3.3	0.875
Tu (%) at the leading edge in Experiment	3.3	0.875
Distance from inflow to plate leading edge (m)	0.25	0.15

For the T3A case, the computational domain begins 0.25 m upstream of the flat plate leading edge and extends across a plate length of 20.0 m. The top boundary is located 5.0 m from the flat plate. In the case of T3A-, the computational domain begins 0.15 m upstream of the flat plate leading edge and extends across a plate length of 2.5 m. The top boundary is located 0.3 m from the flat plate. The boundary conditions used in both cases are the following: nozzle inlet condition with specified total pressure corresponding to the freestream Mach number at the inlet, a Riemann characteristic top boundary, a constant-pressure outflow boundary condition ($\frac{P}{P_\infty} = 1.0$), symmetry on the bottom boundary upstream of the flat-plate leading edge and viscous, adiabatic wall on the plate.

The size of the grids used for the two conditions are given in Tables 2 and 3. The first five levels of mesh used for the T3A case were provided by the AIAA Transition Modeling and Prediction workshop committee. In these grids, the number of grid points doubles with each level. The remaining three were generated by the authors, using the same refinement approach to have additional levels of grids to verify asymptotic convergence. For reference, the fifth mesh level had a near-wall spacing of 1.25 x 10^{-5} m that corresponded to a $y^+ \approx 0.5$ (estimated based on the flat plate boundary-layer theory at the transition onset

location). In the case of grids used for the T3A- condition (listed in Table 3), the grid size doubled between consecutive even or odd levels and each even level grid was obtained through uniform refinement with a factor of 4/3 from the previous odd level grid. The fifth mesh level in this case had a near-wall spacing of 4.00 x 10^{-6} m that corresponded to a $y^+ \approx 0.25$ (estimated based on the flat plate boundary-layer theory at the transition onset location).

Table 2. T3A flat plate mesh dimensions.

Mesh Level	No. of points in streamwise direction	No. of points in wall-normal direction	Points upstream of leading edge
Mesh 1	45	25	13
Mesh 2	89	49	25
Mesh 3	177	97	49
Mesh 4	353	193	97
Mesh 5	705	385	193
Mesh 6	1409	769	385
Mesh 7	2817	1537	769
Mesh 8	5633	3073	1537

Table 3. T3A- flat plate mesh dimensions.

Mesh Level	No. of points in streamwise direction	No. of points in wall-normal direction	Points upstream of leading edge
Mesh 1	181	97	49
Mesh 2	241	129	65
Mesh 3	361	193	97
Mesh 4	481	257	129
Mesh 5	721	385	193
Mesh 6	1961	513	257
Mesh 7	1441	769	385
Mesh 8	1921	1025	513
Mesh 9	2881	1537	769

The skin-friction coefficient experimental data were available for the T3A and T3A- cases and will be used for assessing the accuracy of the model. Velocity profiles are also available at select locations from the experiments and will be used when data are prepared to be listed in the Turbulence modeling resource for a more rigorous validation. While the transition onset location would appear to be a natural metric choice for doing the verification, there is no universally accepted and consistent way of identifying it from CFD computations (turbulence index [26] or the start of C_f rise could be good indicators, but are not completely reliable for all of the problems [39]). Therefore, drag coefficients, and discrete values of the skin-friction coefficient at multiple points around the transition region will be used to check the consistency of the implementation of the LM models between the two codes. The locations for obtaining the point values of skin-friction coefficient are chosen to be: one in the laminar region before the transition onset, one in the middle of the transition zone and one in the turbulent region beyond the end of the transition zone. These locations for the two cases are given in Table 4.

In Fig. 1, grid convergence of the skin-friction coefficient is shown for the T3A case computed using the OVERFLOW and FUN3D codes. Results from both codes appear to be visually grid converged at levels three and above of the mesh family. Comparison of the streamwise evolution of skin-friction obtained with the two codes on mesh level seven against data from the experiment is provided in Fig. 2. There appears to be small differences between the results from the two codes in the transition zone ($1.5E5 \leq Re_x \leq 2.5E5$), but otherwise they closely match each other. However, the results produced by the LM model do not match the experimental data in the transition zone and fails to capture the peak skin-friction levels seen near the termination of the transition zone. These results are also substantially different

to those included in the work by Langtry and Menter [17] that originally described the model. A possible explanation for this is given in Section IV.

Table 4. Locations for obtaining the point values of C_f.

Case	Re_x		
	Laminar region	Transition region	Turbulent region
T3A	5.0E4	2.0E5	5.0E5
T3A-	1.5E6	1.9E6	2.5E6

Figure 3 presents the convergence of the T3A results in terms of the chosen metrics. While the drag coefficient and point values of C_f in the laminar and turbulent regions indicate the results from the two codes converging toward the same value in a monotonic trend, the use of C_f in the middle of a transition zone does not indicate a clean consistent trend. With grid refinement, the differences do appear to narrow, indicating a reduction in error. Although not shown here, a metric involving integration of C_f at a set of uniformly distributed points within the transition zone indicated to a similar trend. From Figs. 3 (a), (b) and (d), it does appear that for mesh level five and above, the differences between the results obtained with the two codes significantly reduces and one needs to establish an optimum error level to declare satisfactory convergence of the results.

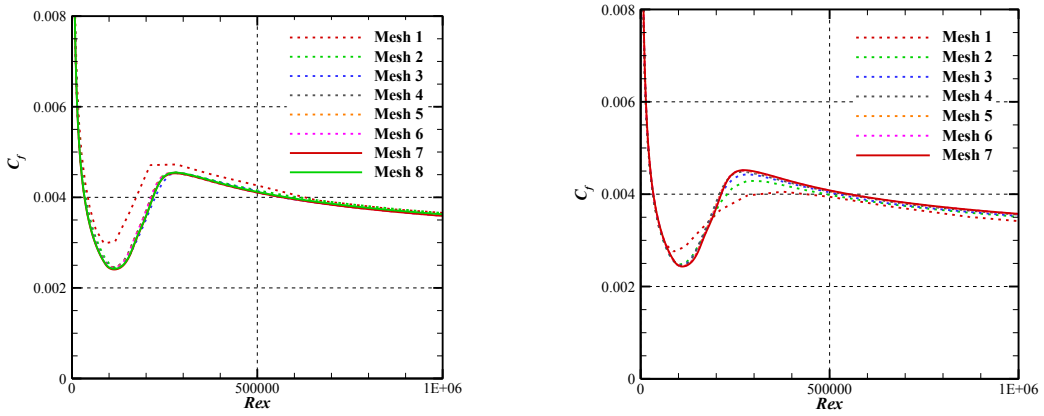

(a) OVERFLOW **(b) FUN3D**

Fig. 1. Comparison of the skin-friction coefficient distribution for different mesh resolutions obtained using the LM implementations in OVERFLOW and FUN3D for the flat plate T3A conditions.

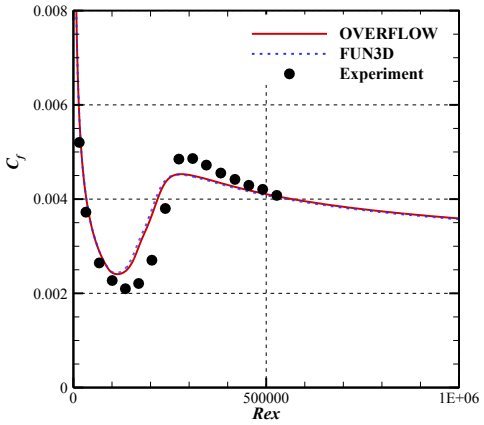

Fig. 2. Comparison of the skin-friction coefficient distribution obtained with the OVERFLOW and FUN3D codes using mesh level 7 against data from experiments for the flat plate T3A conditions.

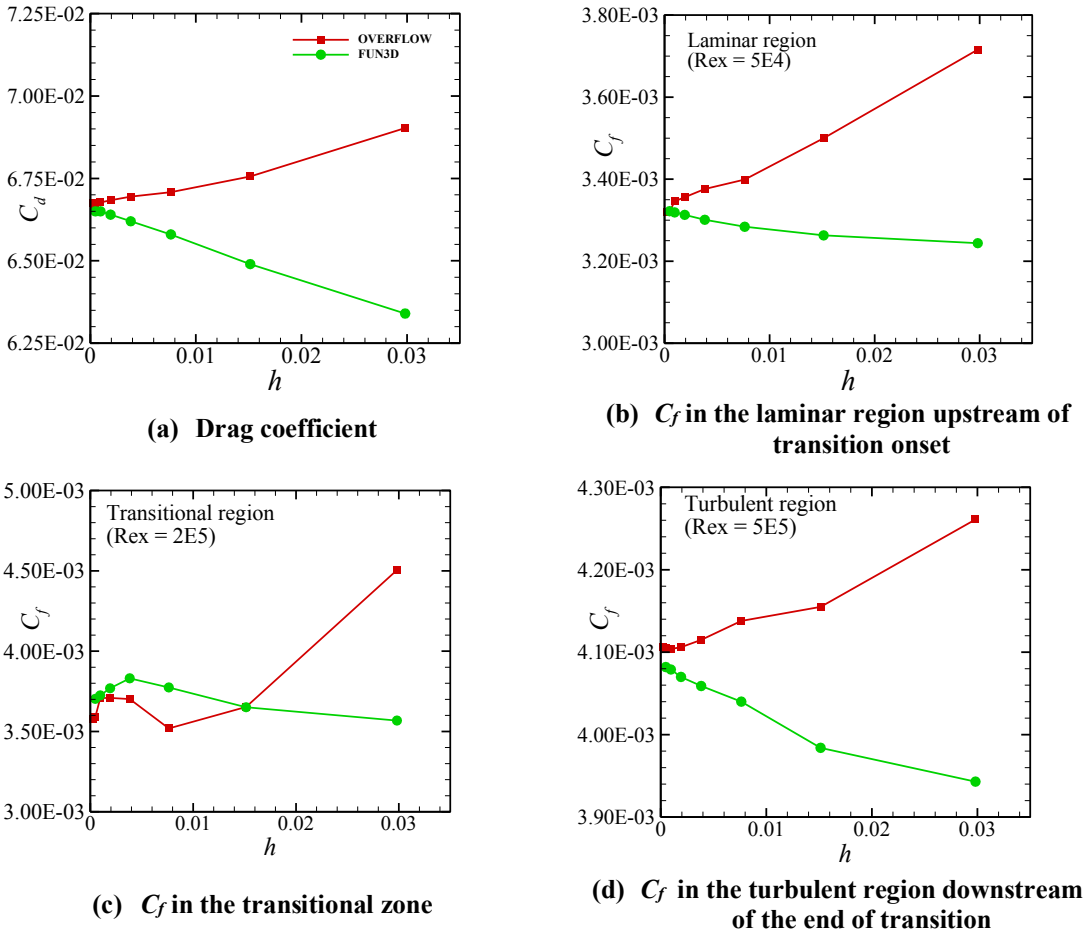

(a) Drag coefficient

(b) C_f in the laminar region upstream of transition onset

(c) C_f in the transitional zone

(d) C_f in the turbulent region downstream of the end of transition

Fig. 3. Plots of grid convergence of the drag coefficient and probed values of the skin-friction coefficient obtained with OVERFLOW and FUN3D for the T3A conditions. Grid sizing parameter $h = 1/\sqrt{N}$.

Plots showing the grid convergence of the streamwise evolution of C_f for the T3A- flow conditions obtained with the two different CFD solvers are given in Fig. 4. OVERFLOW results indicate grid convergence at mesh levels above three, whereas FUN3D approaches grid convergence at mesh levels above five, which may be due to FUN3D being second-order accurate. Comparison of the streamwise evolution of skin-friction obtained with the two codes on the finest mesh against data from the experiments is provided in Fig. 5. As in the T3A case, there appears to be small differences in the results from the two codes within the transition zone ($1.8E6 \leq Re_x \leq 2.1E6$), but otherwise they closely match each other. Also, the transition onset occurs upstream of the location predicted in the experiment.

Figure 6 presents the convergence of the T3A- results in terms of the chosen metrics. Based on Fig. 6(a), results from both codes appear to be approaching different values as the grid is refined, the differences however being in the scale of 8E-5. The same behavior is also seen in the evolution of the point values of C_f obtained in the laminar and transition regions. However, in the turbulent region, the results from both codes approach to the same value. While based on the skin-friction coefficient plot, the results appear to be closer to each other, the trends seen in Figs. 6(a) and (d) need further investigation.

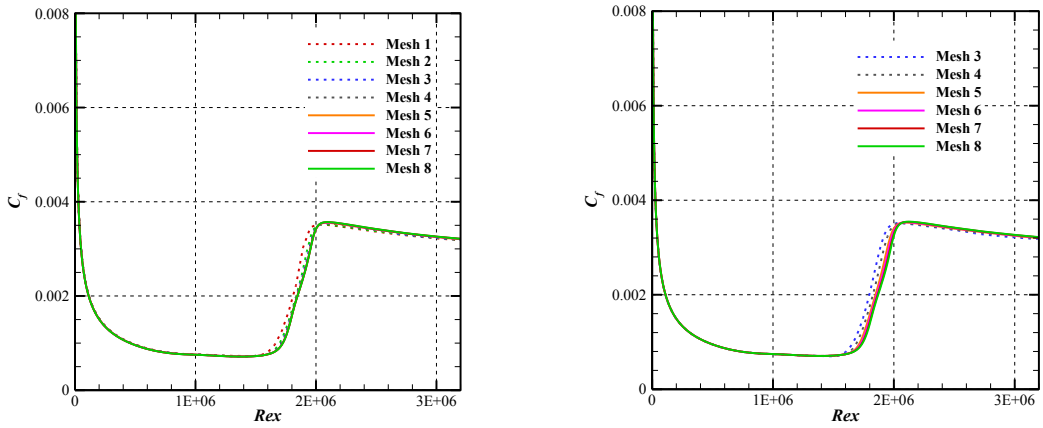

(a) OVERFLOW (b) FUN3D

Fig. 4. Comparison of the skin-friction coefficient distribution for different mesh resolutions obtained using the LM implementations in OVERFLOW and FUN3D for the flat plate T3A- conditions.

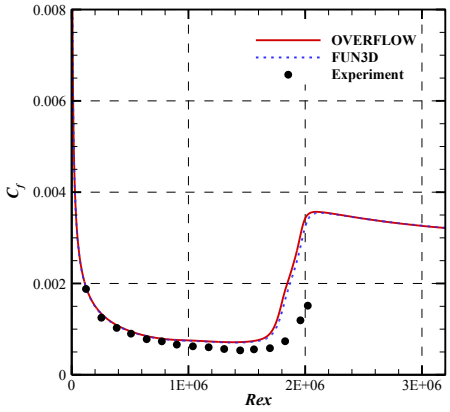

Fig. 5. Comparison of the skin-friction coefficient distribution obtained with OVERFLOW and FUN3D on the finest mesh against data from experiments for the flat plate T3A- conditions.

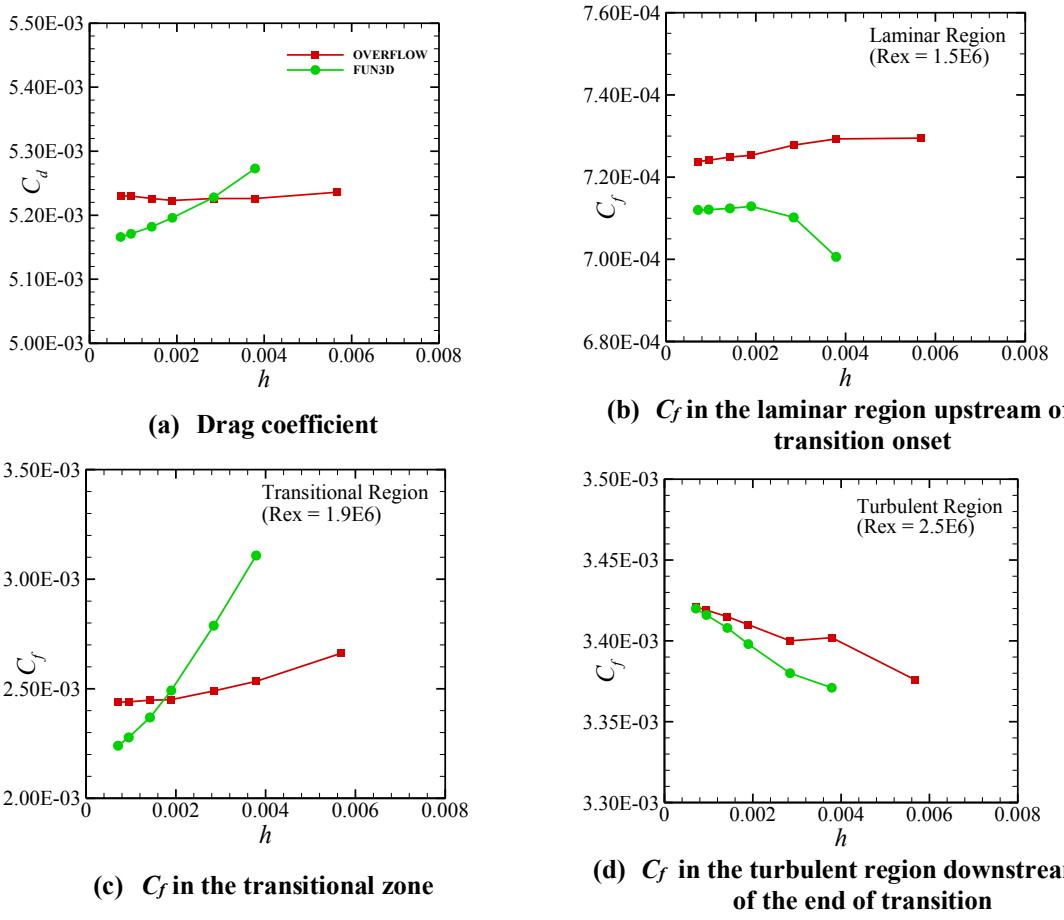

Fig. 6. Plots of grid convergence of the drag coefficient and probed values of the skin-friction coefficient obtained with OVERFLOW and FUN3D for the T3A- conditions.

B. Natural Laminar Flow Airfoil, NLF(1)-0416: Low Reynolds Number Case

The NLF(1)-0416 airfoil is a natural laminar flow configuration that was developed at the NASA Langley Research Center by D. Somers [32]. It is designed for general aviation applications to achieve a high value of the maximum lift coefficient and a low cruise drag coefficient. Reference. [32] provides further information on the geometry and experimental test conditions, as well as the measured results. The flow condition studied herein corresponds to $M_\infty = 0.1, Re_c = 4 \times 10^6$, $c = 1$ m, $\alpha = 0°$ and $5°$, and $T_\infty = 300$ K, as specified for the AIAA Transition Modeling and Prediction workshop.[***] The freestream turbulence intensity in the experiment was 0.15%. For $\alpha = 0°$, the onset of transition is triggered by Tollmien-Schlichting (TS) instabilities on the upper and lower surfaces of the airfoil. At $\alpha = 5°$, transition is triggered by TS instabilities on the upper surface of the airfoil, whereas transition on the lower surface is induced by a laminar separation bubble.

The size of the grids used for the two conditions are given in Table 5. The first six levels of meshes listed were provided by the AIAA Transition Modeling and Prediction workshop committee, and the number of grid points doubles with every other level. The grid was of C-type and generated using a conformal mapping method. The farfield boundary was placed 1000 chords away from the airfoil surface. The additional grids listed in Table 5 were generated, using the same refinement approach, to verify asymptotic convergence. For reference, the fifth mesh level had a near-wall spacing of approximately

[***] https://transitionmodeling.larc.nasa.gov/wp-content/uploads/sites/109/2020/02/TransitionMPW_CaseDescriptions.pdf

1.55×10^{-6} chords corresponding to a $y^+ \sim 0.2$ (estimated based on the flat plate boundary-layer theory at the midchord location), with the spacing near the leading edge and trailing edge being 0.0005 chords and 0.00025 chords, respectively.

Table 5. NLF(1)-0416 mesh dimensions.

Mesh Level	No. of points in chordwise direction	No. of points in wall-normal direction	No. of points in wake-cut
Mesh 1	353	49	49
Mesh 2	529	73	73
Mesh 3	705	97	97
Mesh 4	1057	145	145
Mesh 5	1409	193	193
Mesh 6	2113	289	289
Mesh 7	2817	385	385
Mesh 8	4225	577	577

All of the results reported here were obtained by using the SST turbulence model with sustaining terms (designated SST-sust2003) to ensure that the turbulence intensity level near the leading edge of the airfoil was 0.15% as was measured in the experiment. As a result, at the inflow/farfield boundary, Tu was specified to be 0.15 % and $\mu_t/\mu = 1.0$ in both CFD solvers.

The pressure coefficient distribution and the location of transition (for both upper and lower surfaces at $\alpha = 0°$ and only for the lower surface at $\alpha = 5°$) available from the experiment were used to assess the accuracy of the model. Here again, the lift and drag coefficients, the viscous component of the drag coefficient, C_{DV} and point values of the skin-friction coefficient at multiple points around the transition region on both the surfaces were used to check the consistency of the implementation of the LM models between the two codes. The point probe locations of the skin-friction coefficient are once again chosen to be one in the laminar region before the transition onset, one in the middle of the transition zone and one in the turbulent region beyond the end of the transition zone. These locations for the two cases are given in Table 6.

Table 6. Locations for obtaining the point values of C_f for NLF(1)-0416 airfoil.

Case	Surface	*x/c*		
		Laminar region	**Transition zone**	**Turbulent region**
$\alpha = 0°$	Upper	0.20	0.41	0.80
	Lower	0.40	0.55	0.80
$\alpha = 5°$	Upper	0.10	0.26	0.80
	Lower	0.40	0.65	0.80

The evolution the pressure and skin-friction coefficient distributions along the airfoil using the different meshes and two CFD solvers are shown in Fig. 7 for $\alpha = 0°$. While the pressure coefficient visually appears to converge quickly within two levels of mesh refinement, achieving grid-converged skin friction coefficient distribution needs higher resolution meshes. OVERFLOW results indicate that mesh level three or higher is needed to obtain reasonably grid-converged results for the C_f evolution on the upper surface and mesh level six or higher for the lower surface. As for FUN3D, on the upper surface the C_f profiles appear to collapse with each other for mesh level 5 and higher whereas the data collapses only for mesh levels seven and eight on the lower surface. Moreover, the results obtained with FUN3D on mesh levels five or lower result in significantly upstream predictions of the transition onset location on the lower surface, with a difference of as much as 20% chord.

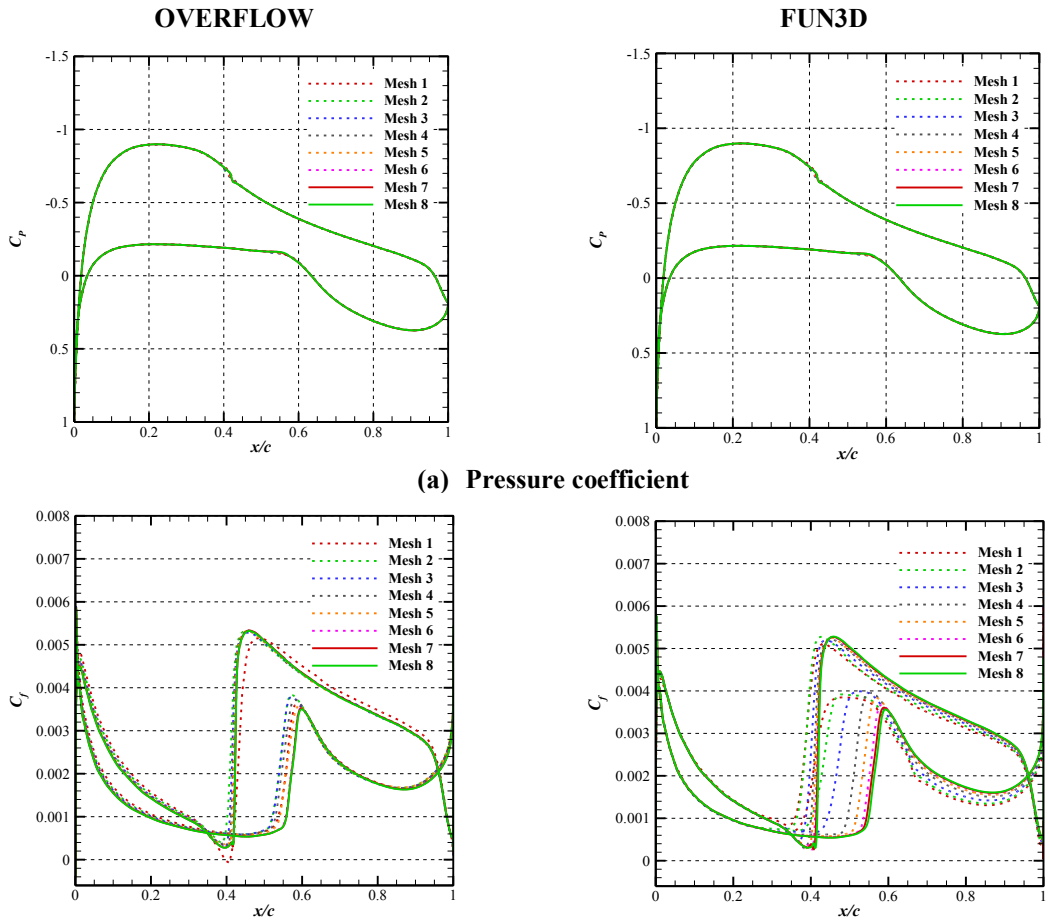

(a) Pressure coefficient

(b) Skin-friction coefficient

Fig. 7. The pressure coefficient and skin-friction distributions for the NLF(1)-0416 airfoil at $Re_c = 4 \times 10^6$, and $\alpha = 0°$.

As displayed in Fig. 8(a), the pressure coefficient distributions obtained on the finest mesh with the two CFD codes match well with each other and with the measured data from the experiment, apart from the slightly higher pressure levels seen in the CFD computations on the lower surface of the airfoil. The comparison of skin-friction distributions is shown in Fig. 8(b), along with a region marked by a gray-colored box indicating where the flow switched from being laminar to turbulent in the experiment. The plot indicates that the predicted transition onset location from the SST-sust2003-LM2009 model from both codes match reasonably well with that from the experiment, apart from the small discrepancy in the results between FUN3D and OVERFLOW in the transition zone on the lower surface of the airfoil. This could be indicative of the need to perform additional computations on meshes with even finer resolution using FUN3D to rule out any grid-convergence related issues.

Plots showing the grid convergence of the lift and drag coefficients, as well as the viscous component of the drag coefficient (in order to isolate the effects of transition from that due to pressure) obtained with the two different CFD codes are given in Fig. 9. These plots clearly indicate that both codes are converging to the same value with mesh refinement for these chosen quantities. As was seen from the plot showing the skin-friction distribution evolution with mesh refinement (Fig. 7(b)), OVERFLOW results are less steep in their asymptotic approach to an infinite grid solution than FUN3D. At mesh level five and higher, the differences between the two codes are significantly smaller.

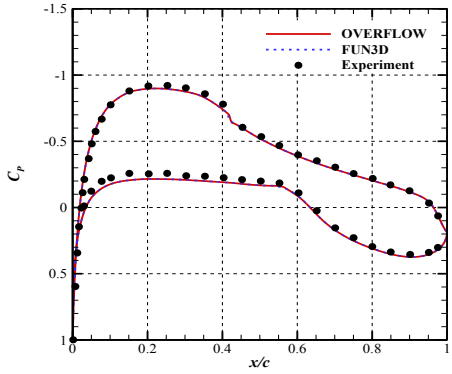

(c) Pressure coefficient

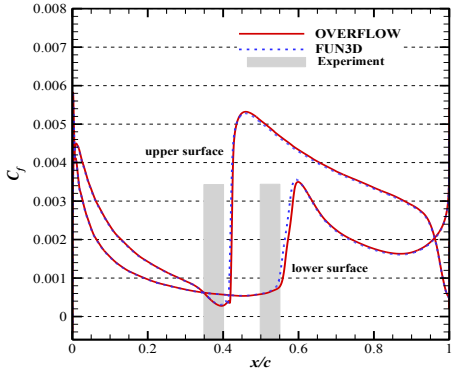

(d) Skin-friction coefficient

Fig. 8. The pressure coefficient and skin-friction distributions obtained with OVERFLOW and FUN3D on the finest mesh against data from experiments for the NLF(1)-0416 airfoil at $Re_c = 4 \times 10^6$, and $\alpha = 0°$.

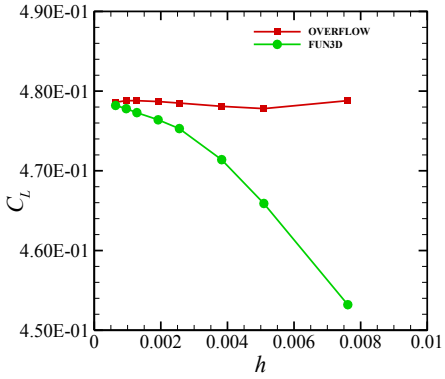

(a) Lift coefficient

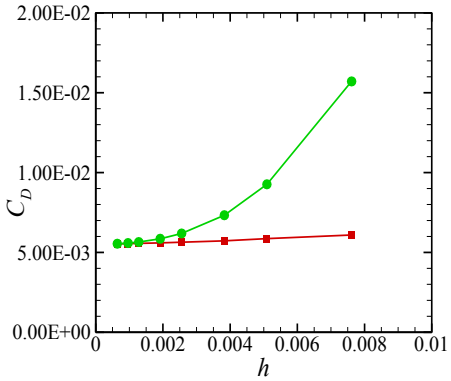

(b) Drag coefficient

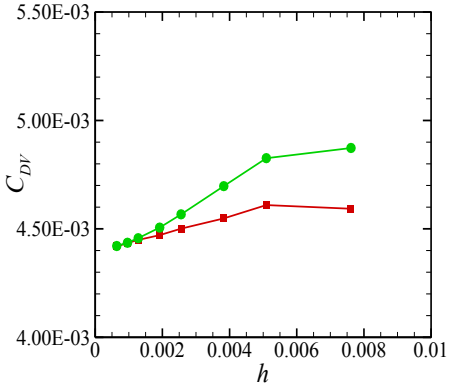

(c) Viscous drag coefficient

Fig. 9. Plots of grid convergence of the force coefficients obtained with OVERFLOW and FUN3D for the NLF(1)-0416 airfoil at $\alpha = 0°$.

Figure 10 presents the convergence in terms of point values of C_f at different locations on the upper and the lower surfaces indicated in Table 6. Unlike what we saw in the case of the flat plate, here consistent trends are seen for all the locations. In the laminar and turbulent portions, results from both codes appear to be converging toward each other at much coarser levels on the upper surface as opposed to that seen on the

lower surface. In regard to the location within the transition zone, one sees a monotonic trend beyond mesh level three or four converging toward the same value.

The results for $\alpha = 5°$ are shown in Figs. 11–14. The evolution the pressure and skin-friction coefficient distributions along the airfoil using the different meshes and two CFD solvers are shown in Fig. 11. The pressure coefficient visually appears to converge within four levels of mesh refinement. However, the skin friction coefficient distribution on the upper surface appears to need a mesh resolution higher than level five to approach a grid-converged result for both codes. Whereas on the lower surface, very small differences are seen between results obtained on mesh levels higher than three, and the SST-sust2003-LM2009 model accurately predicts the separation bubble induced transition in both codes. This aspect is also evident from the good match between the pressure coefficients obtained with both codes and that from the experiment shown in Fig. 12(a) as well as the perfect overlap in the C_f curves from the two codes along with the location of transition from the experiment on the lower surface (marked by a gray-colored box).

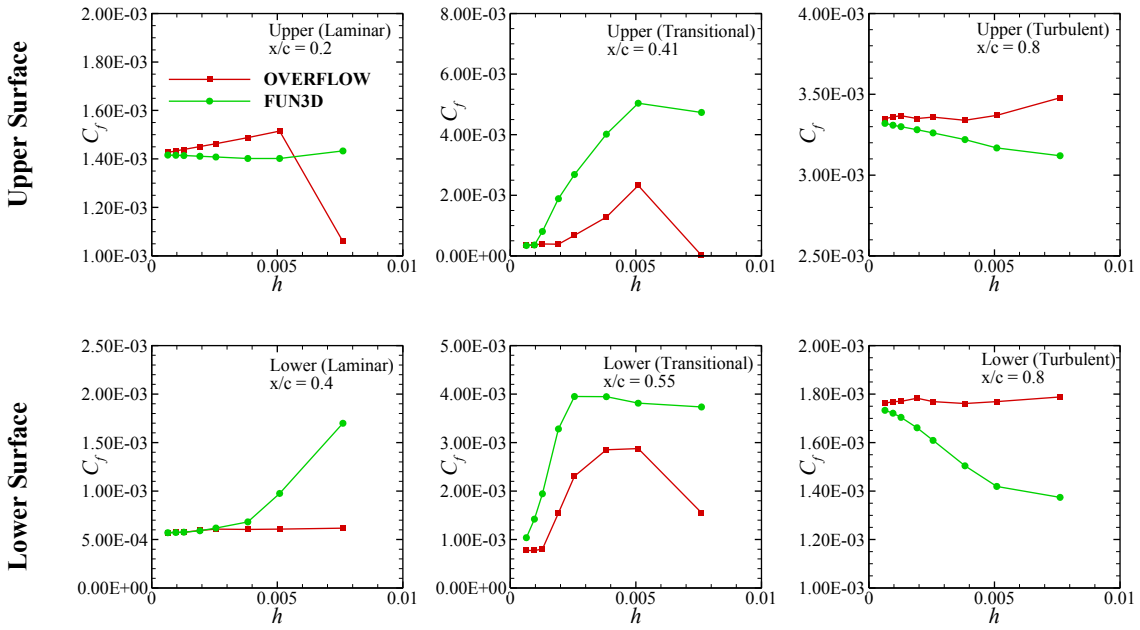

Fig. 10. Illustration of the grid convergence of the probed values of the skin-friction coefficient obtained with OVERFLOW and FUN3D for the NLF(1)-0416 airfoil at $\alpha = 0°$.

Plots showing the grid convergence of the lift and drag coefficients, as well as the viscous component of the drag coefficient obtained with the two different CFD codes are given in Fig. 13. As was seen for the case of $\alpha = 0°$, for this flow condition also, both codes appear to be converging to the same value with mesh refinement for the chosen quantities.

In regard to the convergence in terms of point values of C_f at different locations on the upper and the lower surface, consistent trends are once again obtained as were seen in Fig. 14. Unlike in the case of $\alpha = 0°$ for the laminar and turbulent portions, both codes appear to need mesh level six or higher to approach reasonable convergence of C_f. Within the transition zone, while both codes approach to the same value on the lower surface, there are still differences on the upper surface, similar to what was seen in Fig.11(b).

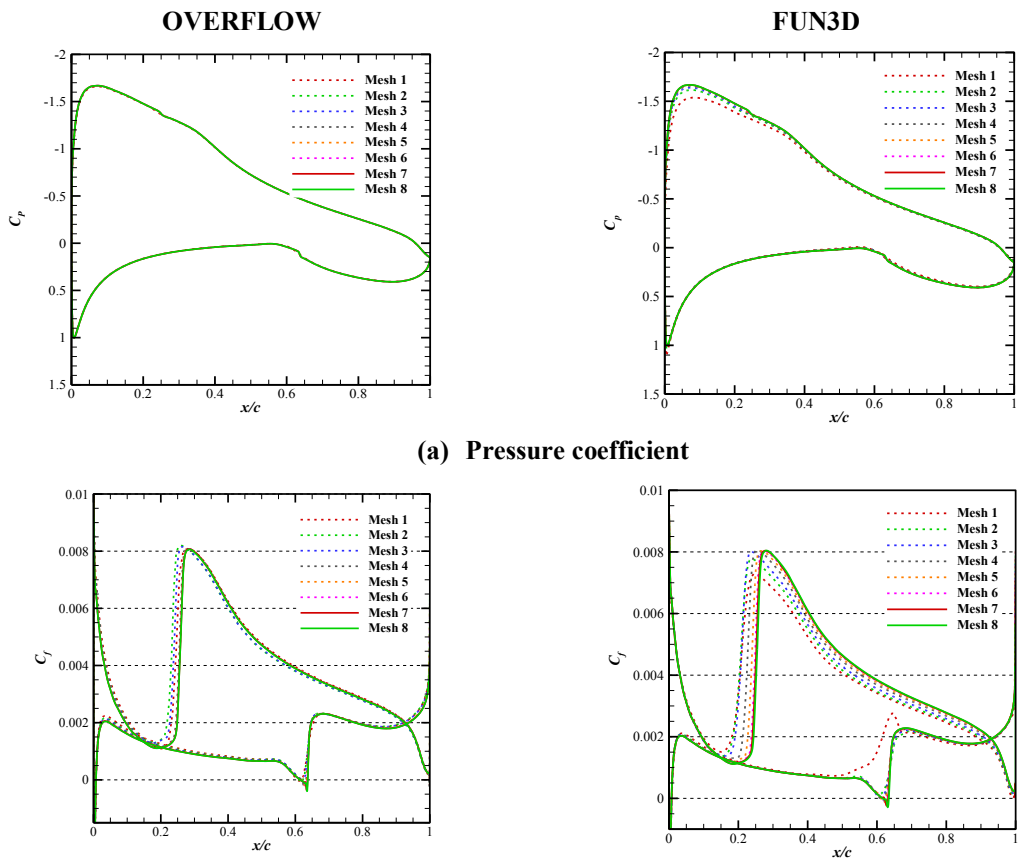

(a) Pressure coefficient

(b) Skin-friction coefficient

Fig. 11. The pressure coefficient and skin-friction distributions for the NLF(1)-0416 airfoil at $Re_c = 4 \times 10^6$, and $\alpha = 5°$.

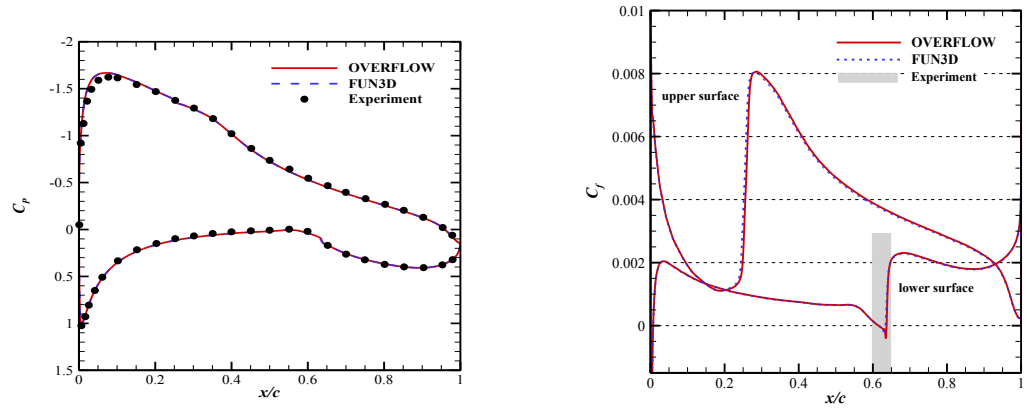

(c) Pressure coefficient **(d) Skin-friction coefficient**

Fig. 12. The pressure coefficient and skin-friction distributions obtained with OVERFLOW and FUN3D on the finest mesh against data from experiments for the NLF(1)-0416 airfoil at $Re_c = 4 \times 10^6$, and $\alpha = 5°$.

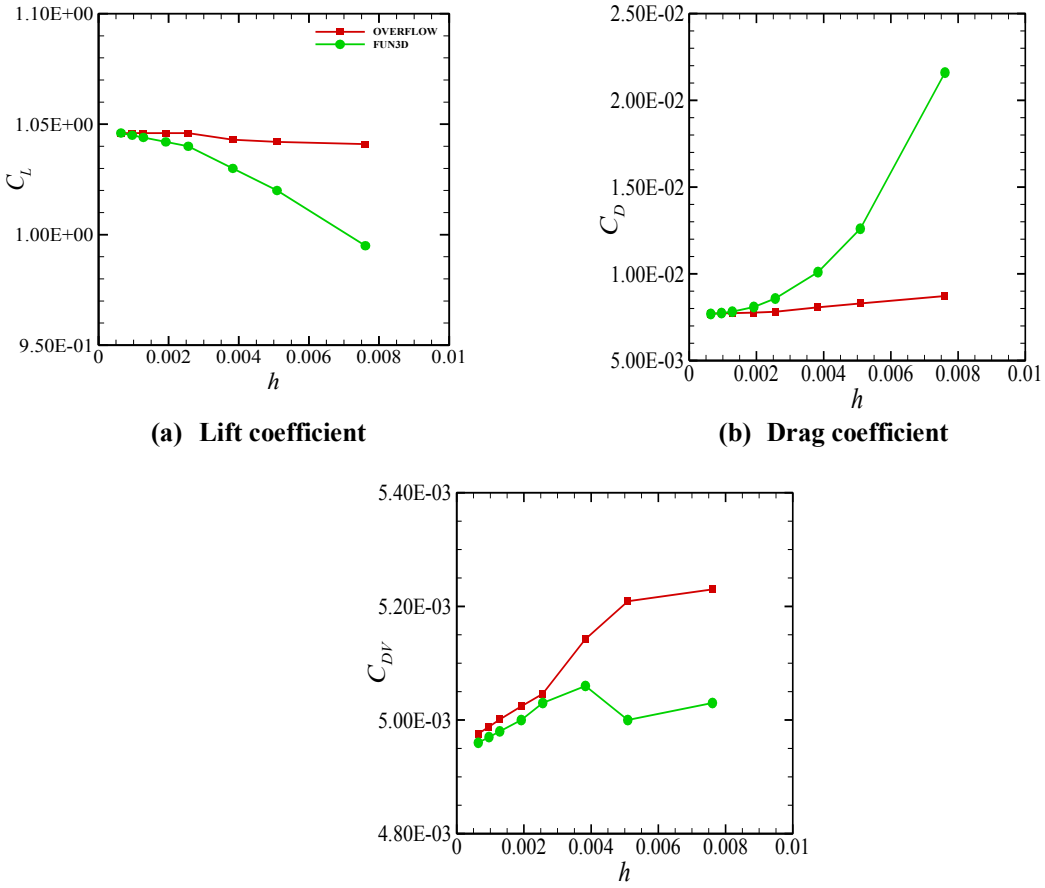

(a) Lift coefficient **(b) Drag coefficient**

(c) Viscous drag coefficient

Fig. 13. Plots of grid convergence of the force coefficients obtained with OVERFLOW and FUN3D for the NLF(1)-0416 airfoil at $\alpha = 5°$.

Overall, the results obtained for the flat plate configuration as well as the NLF(1)-0416 airfoil shown in this section provide satisfactory evidence that there is some consistency in the implementation of the LM model within these two codes. While the flat plate case indicated some inconsistencies in the grid convergence behavior of the skin-friction coefficient in the transition zone, in terms of the other metrics investigated, one has reasonable evidence to believe in the verification of these two codes. The differences seen within the transition zone as well as in some of the other metrics need to be investigated further to check whether they were due to differences in the numerics employed within these codes.

IV. Sensitivity to Model Implementation Specifics and Boundary Conditions

The results of the SST-2003-based LM model can be significantly influenced by variations in the underlying turbulence models, use of limiters, and the specified inflow conditions, especially for Tu and μ_t/μ. This section highlights two such aspects in the context of the flat plate and the NLF(1)-0416 airfoil.

A. Influence of variations in the baseline turbulence model

There is some confusion in the literature regarding the baseline turbulence model with which the LM model needs to be implemented. Many papers refer to the original SST model, but it must be emphasized that the LM model needs to be implemented using the SST-2003 version of the turbulence model.

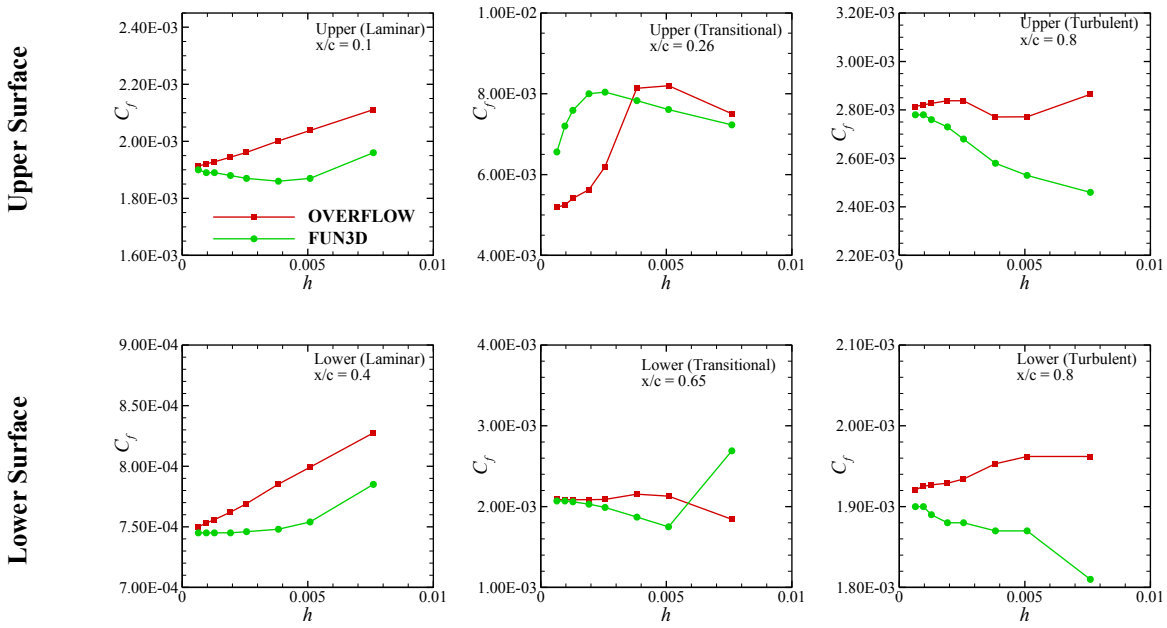

Fig. 14. Plots of grid convergence of the probed values of the skin-friction coefficient obtained with OVERFLOW and FUN3D for the NLF(1)-0416 airfoil at α= 5°.

However, within the SST-2003 model, it is possible to inadvertently use a certain variation as some of the CFD codes by default implement these variants. A comprehensive list and details about the variants can be found in the NASA turbulence modeling resource.

Here we show the impact from two specific variants as applied to the NLF(1)-0416 case at α= 0°. The first variation is the SST-2003 model with the vorticity source term, denoted as SST-V2003, and the second one is the SST-2003 model with the Kato-Launder source term, denoted as SST-KL2003. In SST-V2003, the production term in the model, given by Eq. (4) is replaced with:

$$P = \mu_t \Omega^2 - \frac{2}{3}\rho k \delta_{ij} \frac{\partial u_i}{\partial x_j} \tag{16}$$

where, $\Omega = \sqrt{2W_{ij}W_{ij}}$, is vorticity magnitude and $W_{ij} = \frac{1}{2}(\frac{\partial u_i}{\partial x_j} - \frac{\partial u_j}{\partial x_i})$. The reason for this formulation is that vorticity magnitude is readily available in most CFD codes and it can help with robustness.

The Kato-Launder correction was originally introduced to remedy the excessive turbulent kinetic energy produced by the SST model near stagnation points [40], via limiting the production term in the model. Langel et al. [41] had pointed out that even if this extra turbulent kinetic energy did not significantly alter the solution in the fully turbulent region, it could still significantly influence the development of a transitional flow. In this variation, the production term takes on the form:

$$P = \mu_t \Omega S - \frac{2}{3}\rho k \delta_{ij} \frac{\partial u_i}{\partial x_j} \tag{17}$$

where the strain-invariant S was defined in Eq. (8). This modification is similar in spirit to the vorticity source term approximation described above.

Given that the results for the NLF-0416 airfoil were obtained by invoking the sustaining turbulence terms, the turbulence models used in this exercise for the LM model need to be denoted as SST-sust2003, SST-Vsust2003, and SST-KLsust2003, respectively. The results obtained with the baseline SST-sust2003 model and these two variants on the finest mesh (Mesh 8) are given in Fig. 15. While the overall pressure coefficient distribution looks to be the same between the results obtained using the baseline model and the

two variants, as seen from Fig. 15(a), the close-up view of the region around transition onset provided in Fig. 15(b) provides a better indication of the model influence. The skin-friction coefficient distribution shown in Fig. 15(c) highlights the significant difference in results arising from the use of these variants in a clearer fashion. Both variants appear to cause a separation bubble on both the upper and lower surfaces. While the shift in transition location on the upper surface is within 5% chord, it is more than 15% chord for the lower surface. Results obtained using SST-KLsust2003 are also different from using SST-Vsust2003 on the lower surface. Such a difference is likely to result in significant differences in the force and moment coefficients. Therefore, different asymptotic values from different codes using the same grids and the same transition model may indicate that different variants were used.

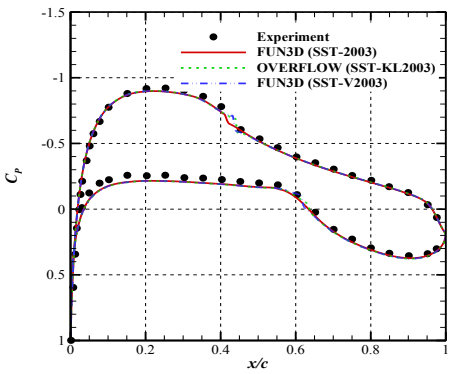

(a) Pressure coefficient

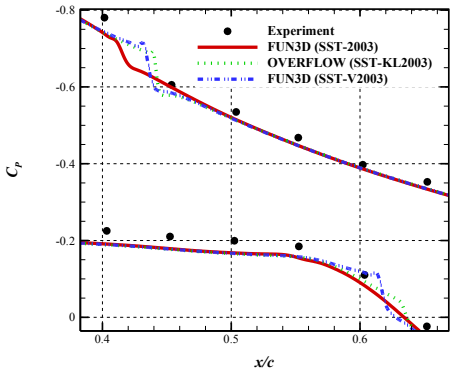

(b) Close-up view of C_P in the region of transition onset

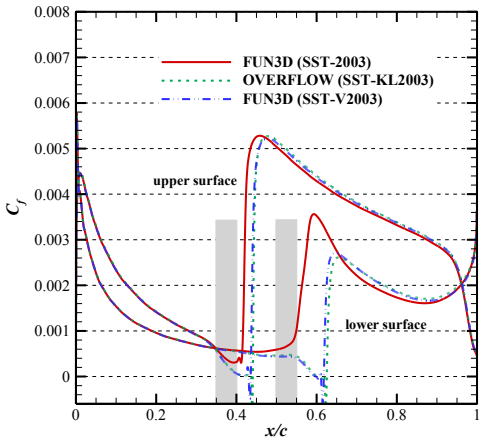

(c) Skin-friction coefficient

Fig. 15. The pressure coefficient and skin-friction distribution obtained using the LM model implemented on top of different variants of the SST-sust2003 turbulence model for the NLF(1)-0416 airfoil at α= 0°.

B. Sensitivity of the LM model to Boundary Conditions

In the Langtry-Menter transition model, the decay of turbulence intensity Tu and turbulent to laminar viscosity ratio $\mu_{tr}=\mu_t/\mu_0$ from the freestream are given by the functions [42]:

$$Tu = Tu_0\left(1+\frac{3\beta Tu_0^2 Re_x}{2\mu_{tr0}}\right)^{-\frac{\beta^*}{2\beta}} \tag{18}$$

$$\mu_{tr} = \mu_{tr0}\left(1 + \frac{3\beta Tu_0^2 Re_x}{2\mu_{tr0}}\right)^{1-\frac{\beta^*}{\beta}} \tag{19}$$

where β*=0.09, β=0.0828, Re_x is the running Reynolds number at the streamwise coordinate x along the plate, and Tu_0 and μ_{tr0} are specified at a reference location x_0. In practice, μ_{tr0} can be derived from measurements of the turbulence intensity decay. The flat plate cases from the ERCOFTAC test series [31] have been benchmark cases for the purpose of transition modeling validation and are some of the few tests for which the turbulence intensity decay was measured upstream of the test article [43]. For example, the zero-pressure gradient T3A test case described in Section IIIA case was used by Langtry and Menter in Ref. [17] to validate their $\gamma - Re_{\theta t}$ two-equation transition model and calibration. In this section, we refer to their simulation as LM09. As indicated before, this test case also served as a basis for the zero-pressure gradient flat plate case of the AIAA 1st Transition Modeling and Prediction Workshop 2021. Table 7 lists the conditions used for LM09 and those prescribed for the transition workshop (and in Section IIIA). In the table, x_0 corresponds to the location of the inflow plane of the computational domain. The leading edge of the plate is located at x=0. The larger inflow turbulence intensity for the workshop case accounts for the turbulence decay over the additional distance from the leading edge, whereas the turbulent to laminar viscosity ratio value of 11.9 was used in both cases. The experimental tests were run at a unit Reynolds number Re_1 of approximately 3.6×10^5/m, as was used for LM09, whereas the workshop case was defined with $Re_1=2\times10^5$/m. In Fig. 16, the decay curves calculated with Eqs. (18-19) for the LM09 and workshop cases are plotted, along with the experimental Tu data. A good agreement is obtained with the turbulence intensity measurements. The turbulent to laminar viscosity ratio μ_{tr} (indicated by dashed lines) is almost 1 unit lower at the leading edge of the plate for the workshop case, compared to the LM09 conditions. The figure also shows that when the distance between the inflow plane and the leading edge is increased from 0.04 to 0.25, the decay curves for the unit Reynolds number 3.6×10^5 can be replicated using the modified inflow boundary conditions Tu_0=22.2% and μ_{tr0}=16.

Table 7. Flow conditions used in the simulations for the T3A flat plate test case.

	Langtry-Menter-2009	**AIAA Transition Workshop**
Inlet Velocity (m/s)	5.4	69.44
Density (kg/m^3)	1.2	0.053
$\mu \times 10^{-5}$ (kg/[m.s])	1.85	1.85
Freestream Temperature (K)	288.17	300.0
Mach Number	0.0159	0.20
Re_1, Unit Reynolds number (/m)	3.60E5	2.0E5
μ_t/μ at inlet (μ_{tr0})	11.9	11.9
Tu (%) at inlet (Tu_0 %)	3.5	5.855
Tu (%) at the leading edge	3.3	3.3
Tu (%) at the leading edge in Experiment	3.3	3.3
x_0, distance from inflow to plate leading edge (m)	0.04	0.25

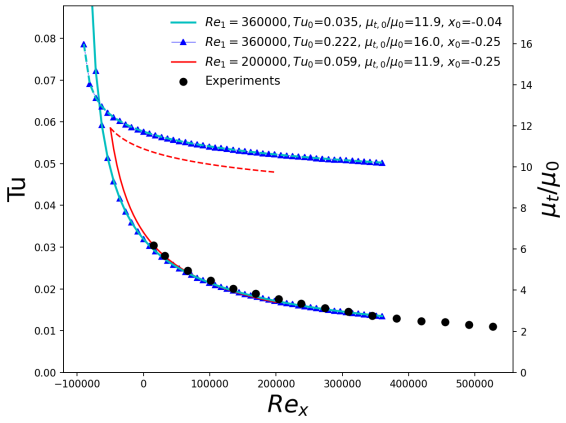

Fig. 16. Turbulence intensity (solid lines) and turbulence to laminar viscosity ratio (dashed lines) decay for different Reynolds numbers and inflow boundaries.

The friction coefficient obtained in OVERFLOW for the T3A case with Mesh level 6 (see Table 2) using different flow and boundary conditions is shown in Fig. 17. The modified inflow conditions set to match the decay curve of Fig. 16 move the transition front downstream, albeit upstream of the measurements and LM09 prediction. The offset to the LM09 result suggests that in the present case, matching the turbulence variable decay curves is not sufficient to adjust for a change in boundary location. A reduction of Tu_0 or μ_{tr0} delays transition, whereas the lower Reynolds number specified for the workshop leads to premature transition. In Ref. [44], it was shown that lowering Tu_0 to 3.5% for the workshop case in combination with μ_{tr0} =17 led to a good agreement with the LM09 result. The dependence of transition predictions on boundary geometry and location with respect to the body will be the subject of a future study.

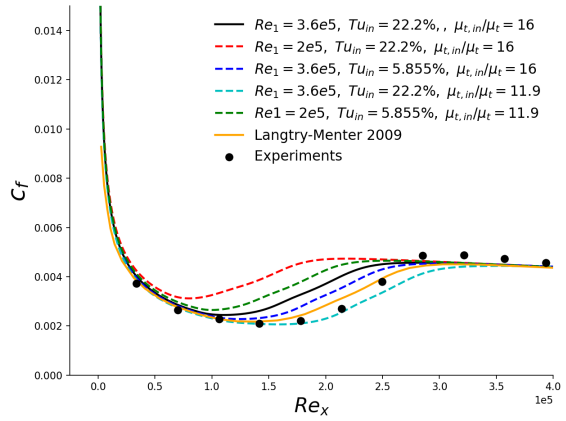

Fig. 17. Friction coefficient on the T3A flat plate for different Reynolds numbers and inflow boundary conditions applied at x_0 = -0.25m.

V. Preliminary Work on Mesh Adaption

In this section, we explore some preliminary ways to adapt the mesh to better suit computations involving transitional boundary layers and should be treated as a work-in-progress. For each of the CFD solvers, a different strategy was attempted.

A. Graded Boundary Layer Meshing Strategy in OVERFLOW

When generating meshes for turbulent flow simulations, it is customary to use a geometric stretching function in the wall-normal direction, with a grid spacing of at most one viscous length scale $\Delta y_1 = y^+$, computed at a selected reference location. The same Δy_1 is used along the complete body surface or a large portion of it, resulting in $\Delta y_1 > y^+$ upstream of the reference location. In this section, we investigate the effect of graded meshing, following the boundary layer growth from the context of the OVERFLOW CFD solver as applied to the T3A flat plate case. A family of 7 grids was generated by increasing Δy_1 along the boundary layer according to a Blasius boundary layer profile, except within the first 0.1m distance from the singular leading edge. Δy_1 was matched with that of the non-graded grid at the location where transition was measured. For both graded and nongraded grids, the first 5 grid spaces were kept constant in the wall-normal direction to better resolve the viscous sublayer of the boundary layer before stretching the mesh. Examples of graded and nongraded grids are shown in Figs. 18 and 19 and the variation in Δy_1 across the length of the plate, for the different grids in these families is shown in Fig. 20. As shown in Figs. 21 and 22, both families of grids converge toward the same asymptotic value. Figure. 22 does not indicate any apparent advantage of grading the mesh in terms of the rate of convergence as a function of the grid size. No systematic advantage was found in rate of iterative of convergence for this particular case. However, further investigation of this approach is needed for cases with a significantly larger laminar region than that investigated here. Furthermore, near-wall grids generated in this way or the adaptive mesh refinement capability inside OVERFLOW [46] may accelerate convergence and help better capture laminar separation bubbles. Different choices of transition and turbulent variables and metrics could be explored to drive the refinement process.

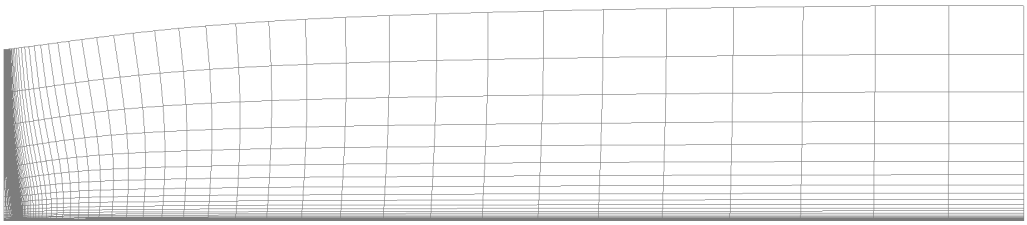

(a) Graded mesh

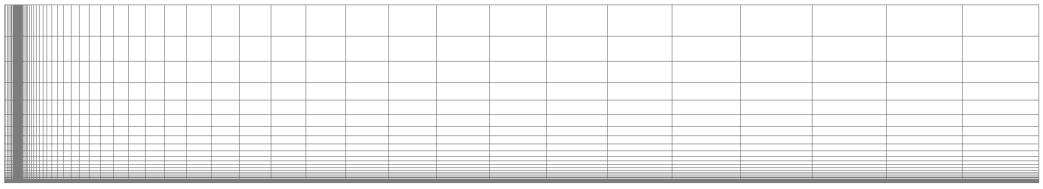

(b) Nongraded Mesh

Fig. 18. Coarse mesh (grid #2) for the flat plate.

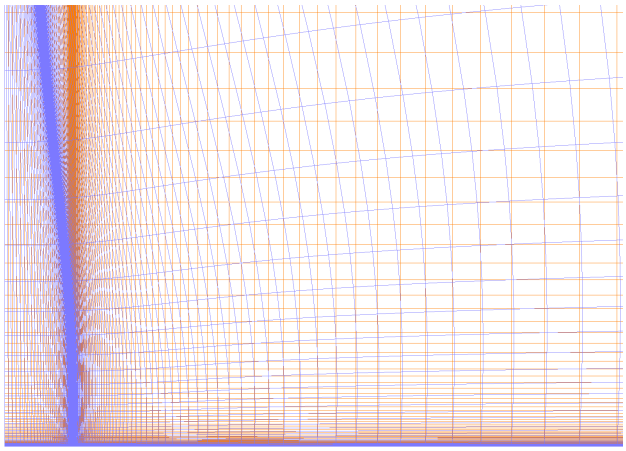

Fig. 19. Close-up of overlaid graded (blue) and nongraded (orange) medium grids (#3) near the plate leading edge.

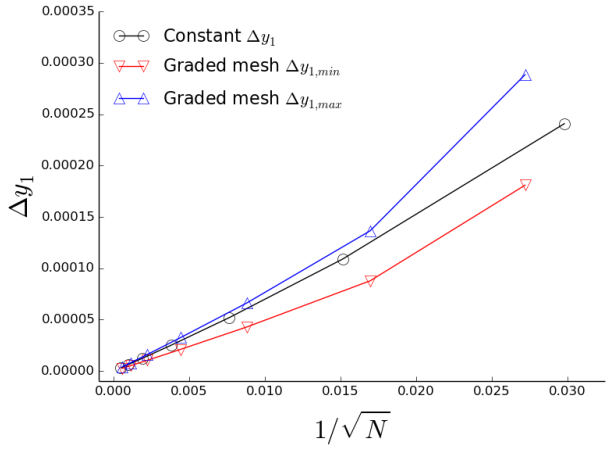

Fig. 20. Minimum and maximum Δy_1 in the graded grids, and constant Δy_1 for the non-graded grids, plotted as a function of the number of mesh nodes N.

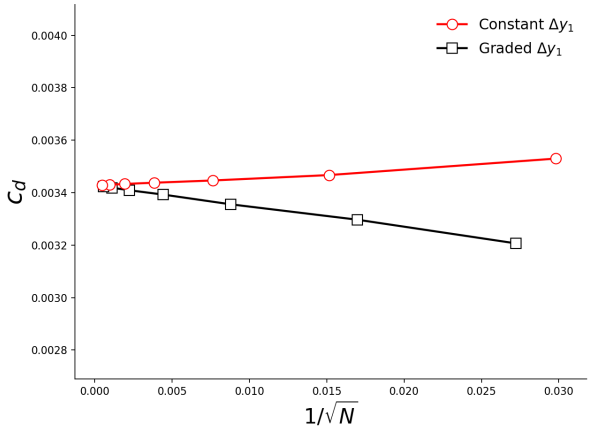

Fig. 21. Drag coefficient as a function of the number of nodes N for the graded and nongraded mesh. The solutions for both grid topologies converge asymptotically toward the same value.

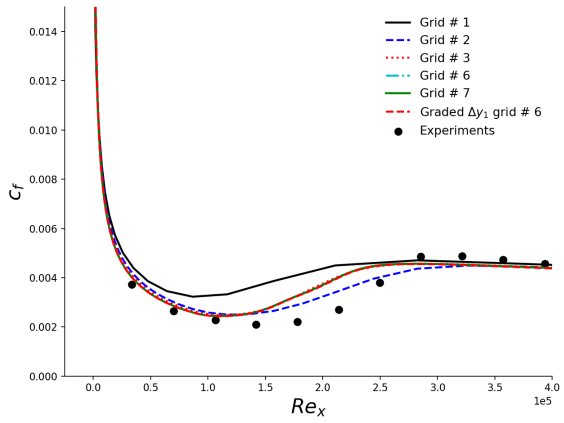

Fig. 22. Friction coefficient for nongraded grids #1, 2, 3, 6, and 7. The solutions converge to the same profile as the graded grid (#6 shown).

B. Sketch to Solution Approach in FUN3D

The anisotropic unstructured metric-based adaptive mesh refinement library known as *refine*[†††] is used with FUN3D to perform mesh adaptation for 2D transitional flows. This process involves multiple steps and is also referred to as sketch to solution (S2S). First, a geometry is created with Engineering Sketch Pad [46]. Next, the user specifies an initial complexity for the computational mesh and the value(s) of Δy^+ along the viscous boundaries. Once the geometry, mesh complexity, and Δy^+ are specified, *refine* generates a baseline grid that best matches all of these requirements. After the baseline grid is created, *refine* starts the adaptive mesh refinement. Additional details about the S2S approach can be found in the work by Kleb et al. [47].

For the adaptive mesh refinement, each FUN3D simulation is run to either a set number of iterations or to iterative convergence. HANIM [48], a strong nonlinear solver in FUN3D, is utilized to improve the iterative convergence of the flow solutions. An estimate of the L^p-norm interpolation error is computed by *refine* from the steady flow solutions. From a user-specified scalar quantity, in this case the Mach number, an anisotropic metric field is constructed. If the error estimate is larger than limits set by the user, then *refine* adapts the current grid to the anisotropic metric field by moving, adding, and/or removing nodes. Once the new grid is created, the previous flow solution gets interpolated onto this grid and used for the flow initialization. Then, the next simulation is run on the new grid. This process continues until either the maximum number of grids for a mesh family is reached or the relative difference in the drag coefficient between the current and last grid is less than a set tolerance. For the adaptive mesh refinement in this work, the maximum number of grids in a family is equal to 10, and the drag coefficient tolerance is 0.001. If either of these criteria are met, the mesh complexity doubles and *refine* continues the adaption.

The multiscale metric field is used for anisotropic mesh adaption while reducing the scalar field's L^p norm of the interpolation error. Lower values of p targets smaller variations in the scalar field, whereas higher values of p targets larger variations. This allows for a balance in the refinement of both the nonsmooth and smooth regions of the scalar field. The multiscale metric field is created from the reconstructed Hessian, which is scaled locally with the Hessian determinant and scaled globally by a complexity correction to produce a target mesh complexity.

In its current state of development, *refine* does not have a transition related metric, such as those based on the operating variables of the SST-2003 turbulence model or the LM model, which can be used to adapt the mesh. As a result, all the results presented here use the Hessian of the Mach number for this purpose, even though it is not ideal. Furthermore, the initial grids developed using this approach have highly

[†††] *refine* is developed by NASA and is available via https://github.com/NASA/refine under the Apache License, Version 2.0.

anisotropic grids that warrant the use of HANIM in FUN3D to achieve convergence, and so far HANIM in FUN3D has only been implemented for the SA turbulence model and does not work with either SST or SST-based LM models. As a consequence, for the demonstration purposes of this paper, all of the results shown have been obtained using the SA turbulence model with the transition location imposed – wherein laminar regions are specified, and turbulent production is turned off within that region. While this approach is not representative of boundary-layer transition-based mesh adaption, as a first step, it does allows for us to see what kind of grids this approach generates and if the meshes get refined in the expected regions around the transition onset.

1. A. T3A Flat Plate

For the first transitional adaptive mesh refinement case**,** we apply *refine* to subsonic flow over a zero-pressure-gradient flat plate with the T3A flow conditions discussed in Section III A. We specify the location of transition onset in FUN3D according to where this location is on Mesh 7 (see Table 2) with the LM model. Results are first computed on the static grids (listed in Table 2) using the SA model with imposed transition. After that, the adaptive mesh refinement is run with *refine*, also using the SA model and imposed transition. The static grids are structured, and the adapted grids are fully unstructured with tetrahedral cells. We compare the simulation results from the static grids and the adapted grids to one another. Each simulation is run to iterative convergence (i.e., residual has reached machine epsilon and has completely leveled out).

Figure 23 shows the grid convergence of the drag coefficient for the FUN3D simulations with the static grids and the adapted *refine* grids. The results from only a single adapted grid for each mesh family of the *refine* procedure are plotted in Fig. 23. For this flat-plate case with T3A conditions, the static grid results for the drag coefficient are more accurate (i.e., closer to being grid converged) on smaller grids than results from the adapted grids. This suggests that *refine* still needs some improvements on adapting the near-wall portion of the computational grid. Both the static grids and the adapted grids are converging to a similar drag coefficient as the grid spacing (h) decreases, but finer grids need to be run in order to determine the actual grid-converged value of the drag coefficient for this case. Figure 24 depicts the grid convergence of the wall skin-friction distribution for the FUN3D simulations with the static grids and the adapted *refine* grids. Also, we include a plot with only the finest grid results on the right in Fig. 24. The number of grid points/cells for each adapted grid and the finest static grid are listed in Fig. 24. Notice as the grid spacing (h) decreases, the adapted grid results approach the finest static grid result in Fig. 24. There are some very minor oscillations in the skin-friction distribution associated with the finest adapted grid that can be seen in the right plot of Figure 24. Nevertheless, the agreement is very good between the finest static grid and the finest adapted grid in terms of skin friction for the flat-plate case. Improvements to how *refine* adapts the near-wall grid should yield better convergence for small grid complexities.

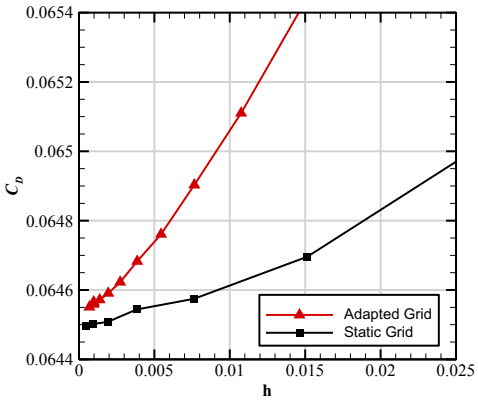

Fig. 23. Convergence of the drag coefficient for the FUN3D simulations of a flat plate with the static AIAA workshop grids and the adapted *refine* grids

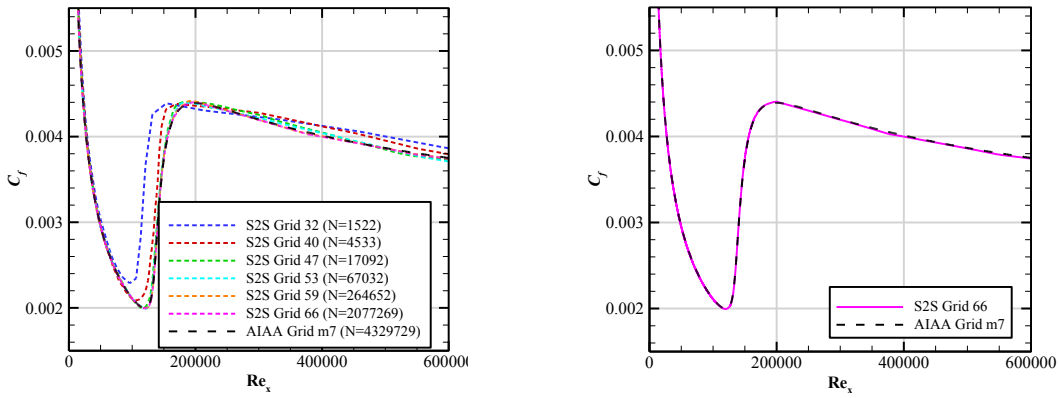

Fig. 24. Convergence of the skin-friction coefficient for the FUN3D simulations of a flat plate with the adapted *refine* grids. A comparison of the mesh level 7 grid (from Table 2) result and the finest adapted grid result is shown on the right.

2. B. NLF(1)-0416 Airfoil

The next transitional adaptive mesh refinement case is the NLF(1)-0416 airfoil with an angle of attack equal to five degrees, which was discussed in section III B. Here again, we employ the SA model with imposed transition. The locations of transition onset for the upper and lower surfaces of the airfoil in FUN3D are set according to where these locations are on the finest static grid (mesh level 8 in Table 5) with the LM model. Both the static grids and the adapted *refine* grids with the SA model and imposed transition are run to iterative convergence. The static grids are structured, and the adapted grids are fully unstructured with tetrahedral cells. Similar to the flat-plate case, we compare the simulation results from the static grids and the adapted grids to one another.

Figure 25 displays the grid convergence of the drag coefficient, the lift coefficient, the pressure-drag coefficient, and the viscous-drag coefficient for the FUN3D simulations with the static grids and the adapted *refine* grids. Unlike the various grid results for the flat-plate case, we see for the NLF-0416 airfoil that as the grid spacing (h) decreases, the drag, lift, and pressure-drag coefficients all converge quicker (i.e., approach the converged value with less grid points/cells) than results from the static grids. For the viscous-drag coefficient in Fig. 25, the trend is the reverse of that seen for the other three force coefficients, with the static grid being slightly more accurate at the coarser level than the *refine* grids. However, they do appear to be approaching close to each other, with the exception that the trend seen on the finest grids shown prevent one from drawing strong conclusions about which grid is better. One can say that the adaptive mesh refinement works very well for the inviscid physics. The total drag and pressure-drag coefficients for both sets of grids converge as the grid spacing decreases. Also, the converged values of these coefficients for the finest static grid and the finest adapted grid match.

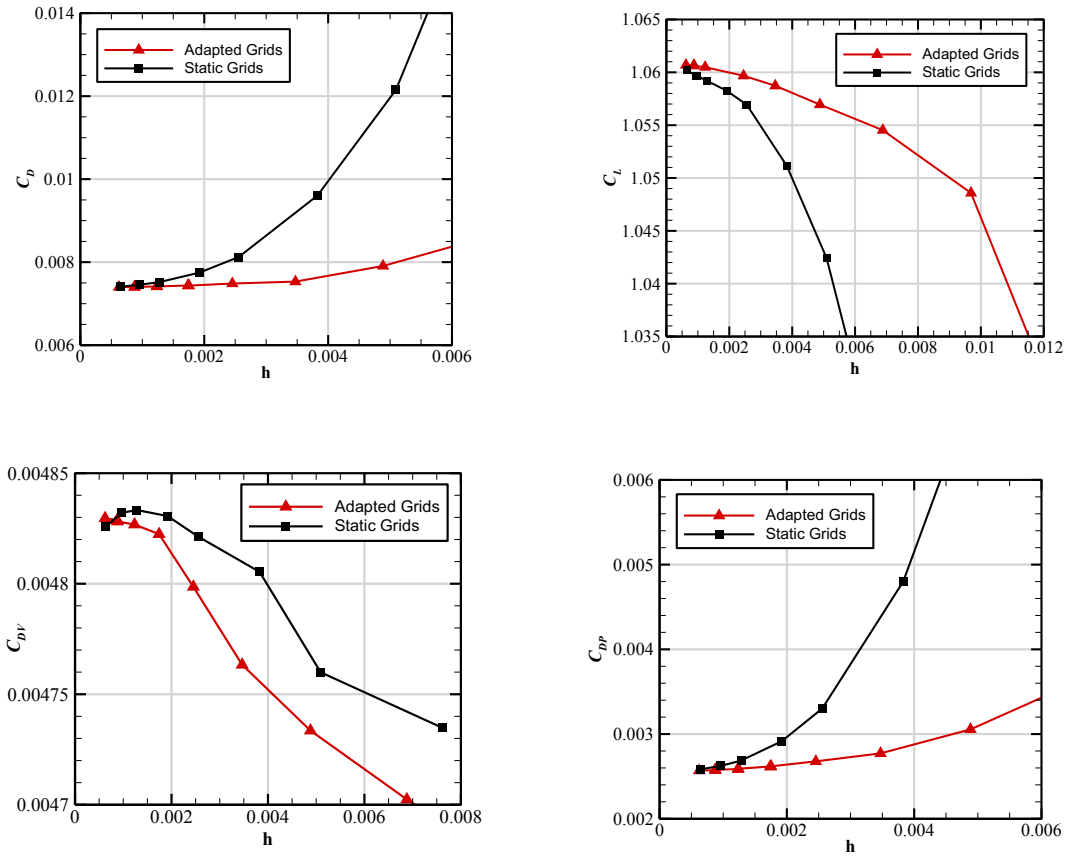

Fig. 25. Convergence of the drag, lift, pressure-drag, and viscous-drag coefficients for the FUN3D simulations of the NLF-0416 airfoil with the static grids and the adapted refine grids.

We show the grid convergence of the skin-friction distributions on the upper and lower surfaces of the NLF-0416 airfoil from the FUN3D simulations with the static grids and the adapted *refine* grids in Fig. 26. The skin-friction distributions have oscillations for the very coarse adapted grid solutions, but they disappear as the number of grid nodes increases from five thousand to 1.3 million. We see in Fig. 26 that as the grid spacing decreases, the adapted grid results approach the finest static grid results. Note that we list the number of grid points/cells for each adapted grid and the finest static grid in Fig. 26. Once the grid complexity is around 3.3×10^5 in *refine*, we obtain good agreement of the skin-friction distributions between the static grids and the adapted grids. Furthermore, the skin-friction distributions from the finest static grid solution and the finest adapted grid solution match very well. Figure 27 displays the pressure coefficient along the upper and lower surfaces of the NLF-0416 airfoil from the FUN3D simulations with the static grids and the adapted grids. We see in Fig. 27 that as the grid spacing becomes smaller, the pressure coefficient distributions from the adapted cases approach the finest static grid result. There are some oscillations in the very coarse adapted grid solutions. Regardless, the agreement is very good between the finest static grid and the finest adapted grid in terms of the coefficient of pressure for the NLF-0416 airfoil transitional case. For this particular airfoil case, *refine* performed better than it did for the flat-plate case.

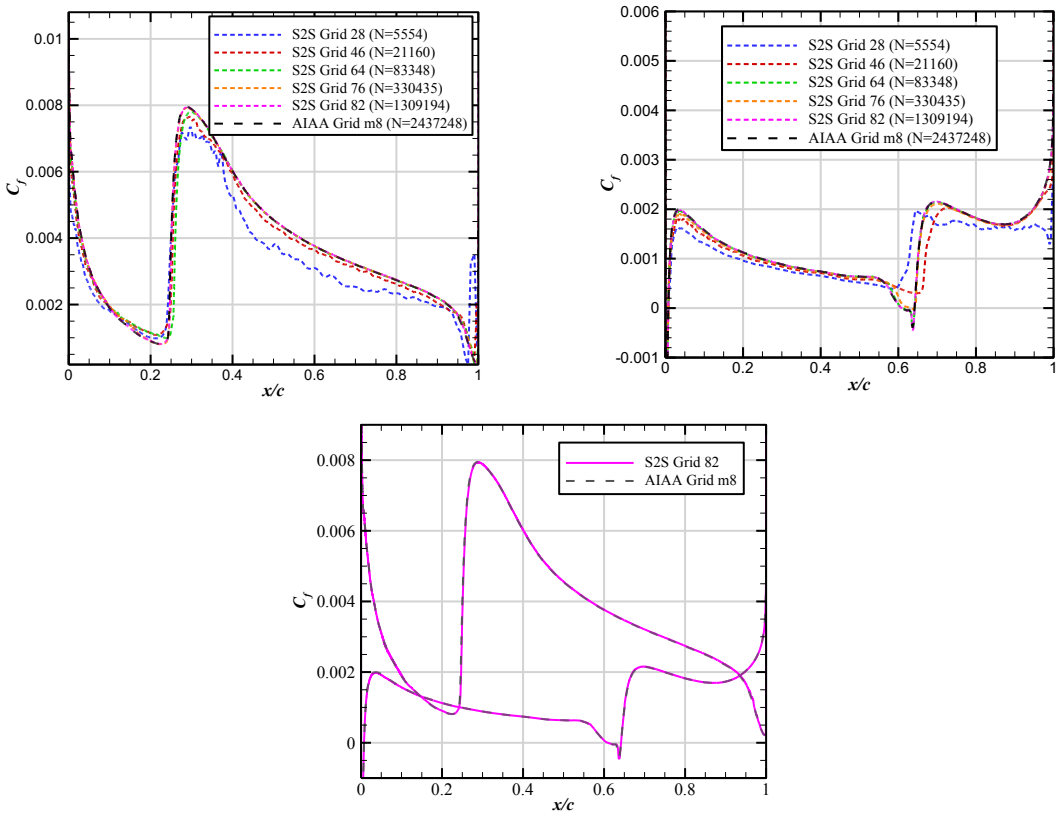

Fig. 26. Convergence of the skin-friction distributions on the upper (top left) and lower (top right) surfaces of the NLF-0416 airfoil from the FUN3D simulations with the adapted *refine* grids. A comparison of the results obtained on mesh level 8 structured grid and the finest unstructured adapted grid is shown on the bottom.

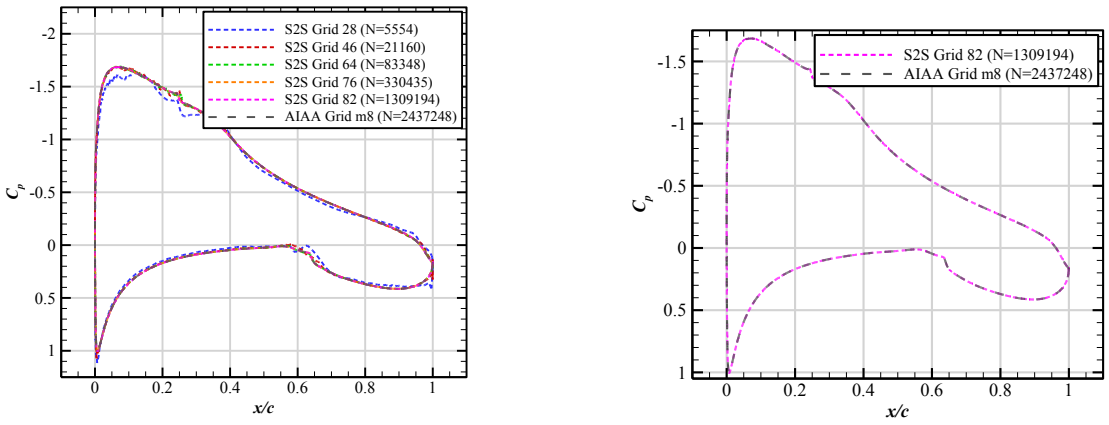

Fig. 27. Convergence of the pressure coefficient for the FUN3D simulations of the NLF-416 airfoil with the adapted *refine* grids. A comparison of the results obtained on mesh level 8 structured grid and the finest unstructured adapted grid is shown on the right.

Now that we have examined the convergence properties of the adaptive mesh refinement with *refine*, we can look at one of the unstructured adapted grids. Figure 28 shows the mesh level six of the structured grid and the 79th adapted *refine* grid near the lower NLF-0416 airfoil surface. Both grids have a similar resolution in the far field and near the lower airfoil surface. The adapted grid has more cells near the leading edge. We can see in Fig. 28 that as the structured grid approaches the lower airfoil surface, it progressively refines in a smooth manner. The unstructured adapted grid in Fig. 28 refines abruptly near the lower surface of the airfoil. Overall, the distribution of tetrahedral cells in the adapted grid is decent. Figure 29 depicts the same grids as Fig. 28, but near the separation bubble region. The magenta lines indicate the streamwise velocity contours in Fig. 29. We again see that as the computational grid approaches the wall, the structured grid refines more smoothly than the unstructured adapted grid in Fig. 29. However, the distribution of points/cells in the immediate vicinity of the separation bubble is roughly the same between the two different types of grids, with the adapted grid having slightly better resolution.

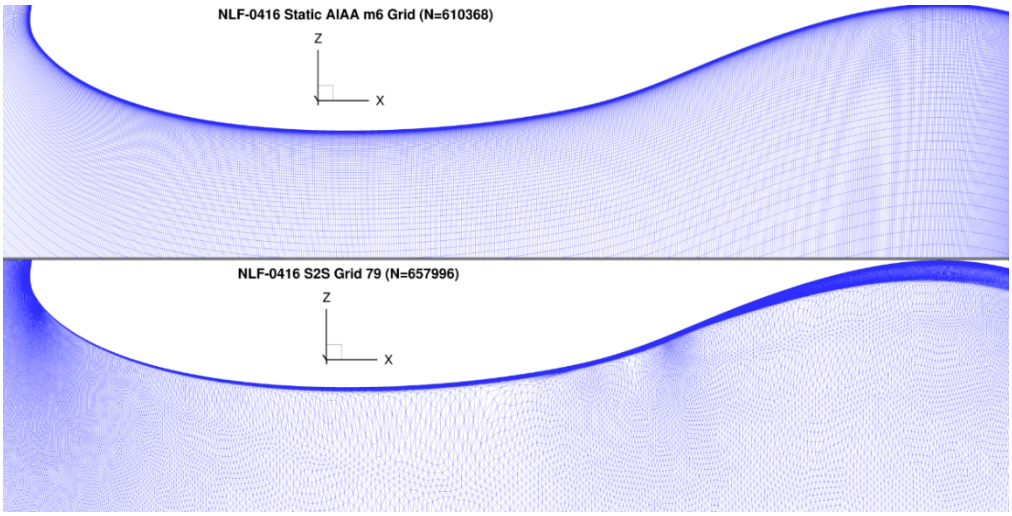

Fig. 28. Visualization of the mesh level 6 of the structured grid and the 79th adapted *refine* grid near the lower NLF-0416 airfoil surface. Part of the far field grid is also shown.

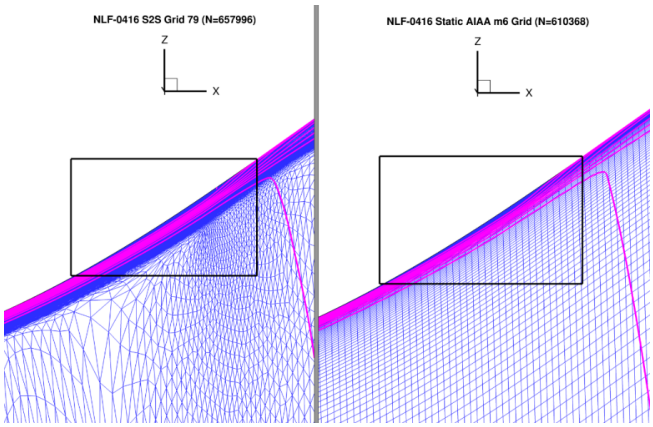

Fig. 29. Visualization of the mesh level 6 of the structured grid and the 79th adapted *refine* grid near the separation bubble that forms on the lower NLF-0416 airfoil surface. The magenta lines indicate the streamwise velocity contours.

Overall, these results indicate that the current application of sketch-to-solution approach needs further improvements in order to capture the transition behavior of boundary layer flows. The immediate approach entails looking into different criteria for adaptation that are specific to such flows.

VI. Concluding Remarks

Transport-equation-based transition models that can be implemented into a RANS framework have gained substantial momentum in recent years due to their simplicity of integration into current parallel CFD programs and their applicability to complex flow geometries. As a result, several workshops have been held to help assess and improve their accuracy, as well as to conduct code-to-code verification. However, even when common spatial grids were used for the workshop flow configurations, there was a large variation in the findings reported by various participants, despite the simple nature of the flow configurations. The lack of agreement between the various computations prevented any significant conclusions about the intrinsic accuracy of these models. An inconsistent implementation of the RANS-based transition models is thought to account for a major part of the variance in CFD predictions. Without truly verified models, it will be difficult to progress toward the evaluation of these models on more complicated flow configurations.

While the CFD research community faced similar issues during the early stages of the AIAA drag prediction workshops, the model verification issue has largely been alleviated for the RANS models through contributions to the NASA Turbulence modeling resource, which provides adequate documentation of the various turbulence models, details related to their implementation, and a set of test problems with grids and solutions to ensure that the models were implemented correctly. The NASA Turbulence modeling resource does also have descriptions of the RANS-based transition models but is currently missing a set of documented test problems along with grids and solutions that would allow for the verification of these RANS-based transition models. The goal of this research is to help code developers in verifying their implementations of the transition models. To facilitate that goal, one must use baseline turbulence models that have been verified and validated and the documentation of the turbulence model V&V effort is available for NASA codes such as OVERFLOW and FUN3D. Because these flow solvers also include some of the most popular transition models, they can be used to generate analogous data for the transition models as well and the findings can be documented in a public resource such as the NASA turbulence modeling resource. To that end, this paper reported our preliminary findings on performing a code-to-code verification of the SST-based Langtry-Menter transition model by applying the aforementioned CFD solvers to two canonical problems, namely, the flat plate configuration from the ERCOFTAC T3 series of experiments and the NLF(1)-0416 airfoil.

The T3A case and the NLF(1)-0416 airfoil configurations were included in the AIAA 1st Transition Modeling and Prediction Workshop (https://transitionmodeling.larc.nasa.gov/workshop_i/), and hence, a family of grids had already been made available to the CFD community by the workshop organizing committee. We have used the same grids and supplemented them with newer grids where necessary. We also investigated an additional flow condition from the T3 series of experiments, namely, T3A-, that was not included in the AIAA workshop. For this case, a new sequence of structured grids was generated, and the solution was validated against the limited data available from the experiments, but the primary focus was on verifying the transition model. The grid convergence of the solution from each of the codes was demonstrated through metrics such as the lift and drag coefficients, as well as comparisons of pressure and skin-friction coefficients. To exemplify the behavior of these models, additional metrics concerning the point values of the skin-friction in the region around the transition zone were used. The comparison of most metrics indicated that the results from the LM model implemented in these two CFD codes was converging to the same value for both the flat plate and NLF-0416 airfoil configurations. The solution metrics predicted by the two solvers indicated a closer agreement for the NLF-0416 airfoil at both angles of attack than similar metrics for the flat plate case at both conditions investigated. In the case of the flat plate, for the T3A conditions, the point value of the skin friction within the transition zone did not yield a consistent trend. For the T3A- condition, with grid refinement, the OVERFLOW and FUN3D predictions for the drag coefficient, as well as the point metric for the skin friction coefficient appeared to diverge from each other, resulting in discrepancies equal to approximately 8E-5. Further work is necessary to identify the source for these discrepancies and to reconcile them. It was observed during the verification of the turbulence models that when a first-order discretization for the convective terms in the turbulence equations in OVERFLOW, the results were in better agreement with the FUN3D predictions [49]. Although the underlying reasons for

this finding remained unknown, it is possible that a similar effect of differences in numerical schemes could account for some of the remaining discrepancies we have observed in the present work.

The sensitivity of LM model predictions to variations in the SST model implementation as well as to the values of important input parameters such as those related to the inflow freestream turbulence was also evaluated. The effect of certain variations in the SST-model implementation on the predictions of the LM model was documented for the NLF-0146 airfoil. Computations for the T3A flat plate established how the Tu and μ_t/μ values at the freestream/inflow boundary can significantly alter the transition onset location. Such shifts in results would adversely impact one's ability to perform model verification and underscore the importance of clearly describing the detailed settings when documenting the results of computations based on the transition models.

Finally, preliminary findings from current work to assess the automatic mesh adaption capabilities of these solvers were reported for flow configurations involving a mix of laminar, transitional, and fully turbulent flows. The approaches taken for the two codes were vastly different from one another. The approach used for the OVERFLOW computations was not fully automated, although it can be automated in the future when combined with the solver's existing mesh-adaption options, whereas the method used in FUN3D was fully automated and produced tetrahedral grids. At this point, no overarching conclusions can be drawn from the effort except that (i) in the case of OVERFLOW, the graded structured meshes did not provide a significant improvement in convergence rates in comparison to grids with uniform wall spacing across the entire domain; and (ii) as the FUN3D's sketch-to-solution approach does not work with the SST-based LM model, it was tested only with the SA model by imposing the transition location. Additionally, *refine* does not have a boundary-layer/transition specific metric and further study is necessary to determine if addressing these aspects would help improve the adapted tetrahedral grids to capture the boundary-layer transition accurately.

Other elements, such as the influence of the order of discretization used for the transition model equations vis-à-vis the order used to solve the mean flow equations, will be investigated in a future study. Extension of the code verification exercise to 3D benchmark problems and also configurations involving crossflow instability through use of specific crossflow related model variants is another remaining task. We aim to expand our work to the SA-based AFT model in the near future. Currently, the AFT model is only implemented in OVERFLOW, but its planned implementation in the FUN3D solver would enable a similar verification as the LM-centric investigation reported in this paper. Eventually, the results from these model verification studies will be released through a publicly available platform such as the NASA's turbulence modeling resource.

Acknowledgments

This research is sponsored by the NASA Transformational Tools and Technologies (TTT) project of the Transformative Aeronautics Concepts Program under the Aeronautics Research Mission Directorate. The research of Balaji Venkatachari is funded by the NASA Langley Research Center through the cooperative agreement 2A00 (Activity 201133) with the National Institute of Aerospace (NIA). The authors thank Chris Rumsey, Mike Park, and Pieter Buning of NASA Langley Research Center for their help through the course of this work. The computing resources used in this work was provided by the NASA Langley Research Center's K-Midrange Cluster and the NASA High-End Computing (HEC) Program through the NASA Advanced Supercomputing (NAS) Division at the NASA Ames Research Center.

References

[1] Lynde, M. N., Campbell, R. L., Rivers, M. B., Viken, S. A., Chan, D. T., Watkins, A. N., and Goodliff, S. L., "Preliminary Results from an Experimental Assessment of a Natural Laminar Flow Design Method," AIAA Paper 2019-2298, 2019.

[2] Lynde, M. N., Campbell, R. L., and Viken, S. A., "Additional Findings from the Common Research Model Natural Laminar Flow Wind Tunnel Test", AIAA Paper 2019-2298, 2019.

[3] Coder, J. G., "Design of a Slotted, Natural-Laminar-Flow Airfoil for Transition Validation Experiments," AIAA Paper 2020-1026, 2020.

[4] Slotnick, J., Khodahoust, A., Alonso, J., Darmofal, D., Gropp, W., and Mavriplis, D., "CFD Vision 2030 Study: A Path to Revolutionary Computational Aerosciences," NASA/CR-2014-218178, 2014.
[5] Smith, A. M. O., and Gamberoni, N., "Transition, Pressure Gradient and Stability Theory," Douglas Aircraft Company, Long Beach, Calif. Rep. ES 26338, 1956.
[6] van Ingen, J. L., "A Suggested Semi-Empirical Method for the Calculation of the Boundary Layer Transition Region," University of Delft, Dept. of Aerospace Engineering, Delft, The Netherlands, Rep. VTH-74, 1956.
[7] Herbert, T., "Parabolized Stability Equations," *Annu. Rev. Fluid Mech.,* 29:245-283, 1997.
[8] Stock, H. W., and Haase, W., "Navier-Stokes Airfoil Computations with e^N Transition Prediction Including Transitional Flow Regions," *AIAA Journal,* Vol. 38, No. 11, 2000, pp. 2059–2066.
[9] Perraud, J., Arnal, D., Casalis, G., Archambaud, J.-P., and Donelli, R., "Automatic Transition Predictions Using Simplified Methods," *AIAA Journal*, Vol.47, No. 11, 2009, pp. 2676-2684.
[10] Krumbein, A., Krimmelbein, N., and Grabe, C., "Streamline-Based Transition Prediction Techniques in an Unstructured Computational Fluid Dynamics Code", *AIAA Journal*, Vol. 55, No. 5, 2017, pp. 1548–1564.
[11] Halila, G. L. O., Fidkowski, K. J., Martins, J. R. R. A., "Toward Automatic Parabolized Stability Equation-Based Transition-to-Turbulence Prediction for Aerodynamic Flows," *AIAA Journal*, Vol. 59, No. 2, 2020, pp. 462–473.
[12] Hildebrand, N., Chang, C.-L., Choudhari, M., Li, F., Venkatachari, B., and Paredes, P., "Coupling of the FUN3D Unstructured Flow Solver and the LASTRAC Stability Code to Model Transition," AIAA Paper 2022-1952, 2022.
[13] Drela, M. and Giles, M. B., "Viscous-Inviscid Analysis of Transonic and Low Reynolds Number Airfoils," *AIAA Journal*, Vol. 25, No. 10, 1987, pp. 1347–1355.
[14] Campbell, R., Campbell, M., and Streit, T., "Progress Toward Efficient Laminar Flow Analysis and Design", AIAA 2011-3527.
[15] Warren, E. S., and Hassan, H. A., "Transition Closure Model for Predicting Transition Onset," *Journal of Aircraft*, Vol. 35, No. 5, September- October 1998, pp. 769-775.
[16] Walters, D. K., and Leylek, J. H., "A New Model for Boundary-Layer Transition Using a Single-Point RANS Approach," *ASME J. of Turbomach*, Vol. 126(1), 2004, pp. 193–202.
[17] Langtry, R. B., and Menter, F. R., "Correlation-Based Transition Modeling for Unstructured Parallelized Computational Fluid Dynamics Codes," *AIAA Journal*, Vol. 47, No. 12, 2009, pp.2894–2906.
[18] Medida, S., and Baeder, J., "Application of the Correlation-based the γ-$\mathrm{Re}_{\theta t}$ Transition Model to the Spalart-Allmaras Turbulence Model", AIAA Paper 2011-3979, 2011.
[19] Langtry, R. B., Sengupta, K., Yeh, D. T., and Dorgan, A. J., "Extending the γ-$\mathrm{Re}_{\theta t}$Correlation based Transition Model for Crossflow Effects," AIAA Paper 2015-2474, 2015.
[20] Fu, S., Wang, L., "RANS modeling of High-Speed Aerodynamic Flow Transition with Consideration of Stability Theory", *Progress in Aerospace Sciences*, Vol. 58, 2013, pp. 36-59.
[21] Coder, J.G., and Maughmer, M.D., "Computational Fluid Dynamics Compatible Transition Modeling Using an Amplification Factor Transport Equation," *AIAA Journal*, Vol. 52, No. 11, 2014, pp.2506–2512.
[22] Coder, J.G., "Further Development of the Amplification Factor Transport Transition Model for Aerodynamic Flows," AIAA Paper 2019-0039, 2019.
[23] Menter, F. R., Smirnov, P. E., Liu, T., and Avancha, R., "A One-Equation Local Correlation-Based Transition Model," *Flow, Turbulence and Combustion*, Vol. 95, No. 4, 2015, pp.583–619.
[24] Menter, F. R., "Two-Equation Eddy-Viscosity Turbulence Models for Engineering Applications," *AIAA Journal*, Vol. 32, No. 8, 1994, pp. 1598-1605.
[25] Menter, F. R., Kuntz, M., and Langtry, R., "Ten Years of Industrial Experience with the SST Turbulence Model," *Turbulence, Heat and Mass Transfer*, Vol. 4 (1), 2003, pp. 625 - 632.
[26] Spalart, P. R. and Allmaras, S. R., "A One-Equation Turbulence Model for Aerodynamic Flows," *Recherche Aerospatiale*, No. 1, 1994, pp. 5-21.
[27] Eca, L., Lopes, R., Toxopeus, S. L., Bettle, M., Rubino, G., Visonneau, M., Venkatachari, B. S., Hilderbrand, N., Choudhari, M. M., Rumsey, C. L., Miozzi, M., Broglia, R., Durante, D., Constantini, M., and Poirier, J. C., "Assessment of Numerical and Modeling Errors of RANS-based Transition Models for Low-Reynolds Number 2D Flows," to be presented at the 34th Symposium on Naval Hydrodynamics, Washington DC, 26 June-1 July, 2022.
[28] Nichols, R. H, and Buning, P. G., "User's Manual for OVERFLOW 2.3, Version 2.3," NASA Langley Research Center, Hampton, VA, Oct 2019.
[29] Biedron, R. T., Carlson, J.-R., Derlaga, J. M., Gnoffo, P. A., Hammond, D. P., Jacobson, K.E., Jones, W. T., Kleb, B., Lee-Rausch, E. M., Nielsen, E. J., Park, M. A., Rumsey, C., Thomas, J. L., Thompson, K. B., Walden, A. C., Wang, L., and Wood, W. A., "FUN3D Manual: 13.7," NASA/TM-0205010139, 2020.
[30] Savill, A. M., "Some Recent Progress in the Turbulence Modeling of By-Pass Transition," *Near-Wall Turbulent Flows*, edited by R. M. C. So, C. G. Speziale, and B. E. Launder, Elsevier, New York, 1993, p. 829.
[31] Roach, P.E. and Brierley, D.H., "The Influence of a Turbulent Free Stream on Zero Pressure Gradient Transitional Boundary Layer Development. Part 1: Testcases T3A and T3B", *Numerical Simulation of Unsteady Flows and Transition to Turbulence*, editors O. Pironneau, W. Rodi, and I. Ryhming, Cambridge University Press, 1992, pp. 319–347.

[32] Somers D. M., "Design and Experimental Results for a Natural Laminar Flow Airfoil for General Aviation Applications," NASA TP-1861, 1981.
[33] Roe, P. L., "Approximate Riemann Solvers, Parameter Vectors, and Difference Schemes," *J. Comput. Phys.,* Vol. 43, No. 2, 1981, pp. 357–372.
[34] Nichols, R. H., Tramel, R. W., and Buning, P. G., "Solver and Turbulence Model Upgrades to OVERFLOW 2 for Unsteady and High-Speed Applications," AIAA Paper 2006-2824, 2006.
[35] Derlaga, J. M., Jackson, C. W., and Buning, P. G., "Recent Progress in OVERFLOW Convergence Improvements," AIAA Paper 2020-1045, 2022.
[36] Anderson, W. K., and Bonhaus, D. L., "An Implicit Upwind Algorithm for Computing Turbulent Flows on Unstructured Grids," *Computers and Fluids*, Vol. 23, No. 1. 1994, pp. 1–21.
[37] Nielsen, E. J., Lu, J., Park, M. A., and Darmofal, D. L., "An Implicit, Exact Dual Adjoint Solution Method for Turbulent Flows on Unstructured Grids," *Computers and Fluids*, Vol. 33, No. 9, 2004, pp. 1131–1155.
[38] Spalart, P. R. and Rumsey, C. L., "Effective Inflow Conditions for Turbulence Models in Aerodynamic Calculations," *AIAA Journal*, Vol. 45, 2022, pp. 683-715.
[39] Carnes, J. A., and Coder, J. G., "Analyzing the Near-Wall Behavior of the Langtry-Menter Transition Model," *Flow, Turbulence and Combustion*, Vol. 108, No. 4, 2015, pp.583–619
[40] Kato, M., and Launder, B., "The Modeling of Turbulent Flow Around Stationary and Vibrating Square Cylinders," *9th Sym. on Turbulent Shear Flows*, Koto, Japan, 1993.
[41] Langel, C.M., Chow, R., van Dam, C.P., "A Comparison of Transition Prediction Methodologies Applied to High Reynolds Number External Flows," AIAA Paper 2016-0551, 2016.
[42] Langtry, R., "A Correlation-Based Transition Model using Global Variables for Unstructured Parallelized CFD Codes", *Ph.D. Thesis*, University of Stuttgart, Germany, May 2006.
[43] ERCOFTAC "Classic Collection" Database, http://cfd.mace.manchester.ac.uk/ercoftac/doku.php?id=cases:case020 (Last accessed April 22, 2022).
[44] Denison, M., "1st AIAA CFD Transition Modeling and Prediction Workshop: OVERFLOW Results for the SST and Langtry-Menter Models", AIAA Paper 2022-0908, 2022.
[45] Buning, P. G., and Pulliam, T. H., "Near-Body Grid Adaption for Overset Grids," AIAA Paper 2016-3326, 2016.
[46] Haimes, R., and Dannenhoffer, J. F., III, "The Engineering Sketch Pad:' A Solid-Modeling, Feature-Based, Web-Enabled System for Building Parametric Geometry," AIAA Paper 2013–3073, 2013.
[47] Kleb, W.L., Park, M. A., Wood, W. A., Bibb, K. L., Thompson, K. B., and Gomez, R. J., "Sketch-to-Solution: An Exploration of Viscous CFD with Automatic Grids," AIAA 2019-2948. 2019.
[48] Wang L., Diskin B., Nielsen E. J., and Liu Y., "Improvements in Iterative Convergence of FUN3D Solutions," AIAA 2021-0857, 2021.
[49] Childs, M. L., Pulliam, T. H., and Jespersen, D. C., "OVERFLOW Turbulence Model Resource Verification Results," NASA Technical Report: NAS-2014-03, 2014.